Euclid Quick Data Release (Q1)

The average far-infrared properties of *Euclid*-selected star-forming galaxies

Euclid Collaboration: R. Hill[*,1], A. Abghari[1], D. Scott[1], M. Bethermin[2], S. C. Chapman[1,3,4], D. L. Clements[5], S. Eales[6], A. Enia[7,8], B. Jego[2], A. Parmar[5], P. Tanouri[1], L. Wang[9,10], S. Andreon[11], N. Auricchio[7], C. Baccigalupi[12,13,14,15], M. Baldi[8,7,16], A. Balestra[17], S. Bardelli[7], P. Battaglia[7], A. Biviano[13,12], E. Branchini[18,19,11], M. Brescia[20,21], S. Camera[22,23,24], G. Cañas-Herrera[25,26], V. Capobianco[24], C. Carbone[27], J. Carretero[28,29], M. Castellano[30], G. Castignani[7], S. Cavuoti[21,31], K. C. Chambers[32], A. Cimatti[33], C. Colodro-Conde[34], G. Congedo[35], C. J. Conselice[36], L. Conversi[37,38], Y. Copin[39], A. Costille[40], F. Courbin[41,42,43], H. M. Courtois[44], M. Cropper[45], A. Da Silva[46,47], H. Degaudenzi[48], G. De Lucia[13], H. Dole[49], F. Dubath[48], X. Dupac[38], S. Dusini[50], S. Escoffier[51], M. Farina[52], F. Faustini[30,53], S. Ferriol[39], F. Finelli[7,54], N. Fourmanoit[51], M. Frailis[13], E. Franceschi[7], M. Fumana[27], S. Galeotta[13], K. George[55], B. Gillis[35], C. Giocoli[7,16], J. Gracia-Carpio[56], A. Grazian[17], F. Grupp[56,57], S. V. H. Haugan[58], W. Holmes[59], I. M. Hook[60], F. Hormuth[61], A. Hornstrup[62,63], K. Jahnke[64], M. Jhabvala[65], B. Joachimi[66], E. Keihänen[67], S. Kermiche[51], A. Kiessling[59], B. Kubik[39], M. Kümmel[57], M. Kunz[68], H. Kurki-Suonio[69,70], A. M. C. Le Brun[71], D. Le Mignant[40], S. Ligori[24], P. B. Lilje[58], V. Lindholm[69,70], I. Lloro[72], G. Mainetti[73], D. Maino[74,27,75], E. Maiorano[7], O. Mansutti[13], S. Marcin[76], O. Marggraf[77], M. Martinelli[30,78], N. Martinet[40], F. Marulli[79,7,16], R. J. Massey[80], E. Medinaceli[7], S. Mei[81,82], M. Melchior[83], Y. Mellier[84,85], M. Meneghetti[7,16], E. Merlin[30], G. Meylan[86], A. Mora[87], M. Moresco[79,7], L. Moscardini[79,7,16], R. Nakajima[77], C. Neissner[88,29], S.-M. Niemi[25], C. Padilla[88], S. Paltani[48], F. Pasian[13], K. Pedersen[89], W. J. Percival[90,91,92], V. Pettorino[25], S. Pires[93], G. Polenta[53], M. Poncet[94], L. A. Popa[95], L. Pozzetti[7], F. Raison[56], R. Rebolo[34,96,97], A. Renzi[98,50], J. Rhodes[59], G. Riccio[21], E. Romelli[13], M. Roncarelli[7], R. Saglia[57,56], Z. Sakr[99,100,101], D. Sapone[102], B. Sartoris[57,13], M. Sauvage[93], M. Schirmer[64], P. Schneider[77], T. Schrabback[103], A. Secroun[51], G. Seidel[64], S. Serrano[104,105,106], C. Sirignano[98,50], G. Sirri[16], L. Stanco[50], J.-L. Starck[93], J. Steinwagner[56], P. Tallada-Crespí[28,29], A. N. Taylor[35], H. I. Teplitz[107], I. Tereno[46,108], N. Tessore[66,45], S. Toft[109,110], R. Toledo-Moreo[111], F. Torradeflot[29,28], I. Tutusaus[106,104,100], L. Valenziano[7,54], L. Valiviita[69,70], T. Vassallo[13,55], G. Verdoes Kleijn[10], A. Veropalumbo[11,19,18], Y. Wang[107], J. Weller[57,56], A. Zacchei[13,12], G. Zamorani[7], F. M. Zerbi[11], I. A. Zinchenko[112], E. Zucca[7], V. Allevato[21], M. Ballardini[113,114,7], M. Bolzonella[7], E. Bozzo[48], C. Burigana[115,54], R. Cabanac[100], M. Calabrese[116,27], A. Cappi[7,117], J. A. Escartin Vigo[56], L. Gabarra[118], W. G. Hartley[48], M. Huertas-Company[34,119,120,121], R. Maoli[122,30], J. Martín-Fleitas[123], S. Matthew[35], N. Mauri[33,16], R. B. Metcalf[79,7], A. Pezzotta[11], M. Pöntinen[69], I. Risso[11,19], V. Scottez[84,124], M. Sereno[7,16], M. Tenti[16], M. Viel[12,13,15,14,125], M. Wiesmann[58], Y. Akrami[126,127], I. T. Andika[128,129], S. Anselmi[50,98,130], M. Archidiacono[74,75], F. Atrio-Barandela[131], D. Bertacca[98,17,50], L. Bisigello[17], A. Blanchard[100], L. Blot[132,71], H. Böhringer[56,133,134], M. Bonici[90,27], S. Borgani[135,12,13,14,125], M. L. Brown[36], S. Bruton[136], A. Calabro[30], B. Camacho Quevedo[12,15,13], F. Caro[30], C. S. Carvalho[108], T. Castro[13,14,12,125], Y. Charles[40], F. Cogato[79,7], S. Conseil[39], A. R. Cooray[137], O. Cucciati[7], S. Davini[19], F. De Paolis[138,139,140], G. Desprez[10], A. Díaz-Sánchez[141], J. J. Diaz[34], S. Di Domizio[18,19], J. M. Diego[142], P.-A. Duc[2], M. Y. Elkhashab[13,14,135,12], A. Finoguenov[69], A. Fontana[30], F. Fontanot[13,12], A. Franco[139,138,140], K. Ganga[81], J. García-Bellido[126], T. Gasparetto[30], V. Gautard[143], E. Gaztanaga[106,104,144], F. Giacomini[16], F. Gianotti[7], A. H. Gonzalez[145], G. Gozaliasl[146,69], M. Guidi[8,7], C. M. Gutierrez[147], A. Hall[35], S. Hemmati[148], C. Hernández-Monteagudo[97,34], H. Hildebrandt[149], J. Hjorth[89], J. J. E. Kajava[150,151], Y. Kang[48], V. Kansal[152,153], D. Karagiannis[113,154], K. Kiiveri[67], J. Kim[118], C. C. Kirkpatrick[67], S. Kruk[38], J. Le Graet[51], L. Legrand[155,156], M. Lembo[85,113,114], F. Lepori[157], G. Leroy[158,80], G. F. Lesci[79,7], J. Lesgourgues[159], T. I. Liaudat[160], A. Loureiro[161,5], J. Macias-Perez[162], M. Magliocchetti[52], E. A. Magnier[32], F. Mannucci[163], C. J. A. P. Martins[164,165], L. Maurin[49], C. J. R. McPartland[63,110], M. Miluzio[38,166], P. Monaco[135,13,14,12], C. Moretti[13,12,14,15], G. Morgante[7], K. Naidoo[144,66], A. Navarro-Alsina[77], S. Nesseris[126], D. Paoletti[7,54], F. Passalacqua[98,50], K. Paterson[64], L. Patrizii[16], A. Pisani[51], D. Potter[157], S. Quai[79,7], M. Radovich[17], G. Rodighiero[98,17], S. Sacquegna[167],

M. Sahlén[168], D. B. Sanders[32], E. Sarpa[15, 125, 14], A. Schneider[157], D. Sciotti[30, 78], E. Sellentin[169, 26], L. C. Smith[170], J. G. Sorce[171, 49], S. A. Stanford[172], K. Tanidis[118], C. Tao[51], G. Testera[19], R. Teyssier[173], S. Tosi[18, 19, 11], A. Troja[98, 50], M. Tucci[48], C. Valieri[16], A. Venhola[174], D. Vergani[7], G. Verza[175], P. Vielzeuf[51], and N. A. Walton[170]

(Affiliations can be found after the references)

September 29, 2025

ABSTRACT

The first Euclid Quick Data Release (Q1) contains millions of galaxies with excellent optical and near-infrared (IR) coverage. To complement this dataset, we investigate the average far-IR properties of *Euclid*-selected main sequence (MS) galaxies using existing *Herschel* and SCUBA-2 data. We use $17.6\,\mathrm{deg}^2$ ($2.4\,\mathrm{deg}^2$) of overlapping *Herschel* (SCUBA-2) data, containing 2.6 million (240 000) MS galaxies. We bin the *Euclid* catalogue by stellar mass and photometric redshift and perform a stacking analysis following `SimStack`, which takes into account galaxy clustering and bin-to-bin correlations. We detect stacked far-IR flux densities across a significant fraction of the bins. We fit modified blackbody spectral energy distributions in each bin and derive mean dust temperatures (T_d), dust masses (M_d), and star-formation rates (SFRs). We find similar mean SFRs compared to the *Euclid* catalogue, and we show that the average dust-to-stellar mass ratios decreased from $z \simeq 1$ to the present day. Average dust temperatures are largely independent of stellar mass and are well-described by the function $T_2 + (T_1 - T_2)\,e^{-t/\tau}$, where t is the age of the Universe, $T_1 = (79.7 \pm 7.4)\,\mathrm{K}$, $T_2 = (23.2 \pm 0.1)\,\mathrm{K}$, and $\tau = (1.6 \pm 0.1)\,\mathrm{Gyr}$. We argue that since the dust temperatures are converging to a non-zero value below $z = 1$, the dust is now primarily heated by the existing cooler and older stellar population, as opposed to hot young stars in star-forming regions at higher redshift. We show that since the dust temperatures are independent of stellar mass, the correlation between dust temperature and SFR depends on stellar mass. Lastly, we estimate the contribution of the *Euclid* catalogue to the cosmic IR background (CIB), finding that it accounts for $> 60\%$ of the CIB at 250, 350, and $500\,\mu\mathrm{m}$. As the *Euclid* mission progresses, larger catalogues will allow us to probe the far-IR properties of MS galaxies out to higher redshifts and lower stellar masses, potentially recovering the complete CIB.

Key words. Galaxies: evolution – Galaxies: star formation – Submillimetre: galaxies – Submillimetre: diffuse background

1. Introduction

The *Euclid* mission (Euclid Collaboration: Mellier et al. 2025) will observe $14\,000\,\mathrm{deg}^2$ of the extragalactic sky, detecting billions of galaxies at optical (with the VIS instrument at 550–900 nm; Euclid Collaboration: Cropper et al. 2025) and near-infrared (with the Near-Infrared Spectrometer and Photometer, NISP at 1–$2\,\mu\mathrm{m}$; Euclid Collaboration: Jahnke et al. 2025) wavelengths. The first Quick Data Release (Q1; Euclid Quick Release Q1 2025) provided single-exposure observations covering three deep fields: Euclid Deep Field Fornax (EDF-F); Euclid Deep Field North (EDF-N); and Euclid Deep Field South (EDF-S). Even at the current depths (about magnitude 24.7 in VIS and 23.2 in NISP) the catalogues generated from these observations contain over 10 million galaxies detected in the *Euclid* filters (Euclid Collaboration: Romelli et al. 2025).

Spectral energy distributions (SEDs) have been fit to the *Euclid*-selected galaxies, providing robust photometric redshifts, stellar masses, and star-formation rates (SFRs) for the majority of the galaxies (Euclid Collaboration: Tucci et al. 2025). This catalogue was recently used to constrain the correlation between the stellar mass (M_*) and SFR of star-forming galaxies (known as the galaxy star-forming main sequence, or MS) out to $z = 3$ (Euclid Collaboration: Enia et al. 2025). The correlation is related to universal processes which have been converting cold gas reservoirs into stars since at least $z = 6$. Because the bulk of the galaxies in the Universe follow the star-forming MS, determining its evolution is crucial for understanding galaxy evolution in general. For example, it is known that the amplitude of the MS increases with redshift for galaxies of all stellar mass (Speagle et al. 2014; Daddi et al. 2022; Popesso et al. 2023), implying that the specific SFRs (sSFRs) of all galaxies were higher in the early Universe. There is also a deviation from a linear trend at high stellar mass, meaning that there is a maximum average SFR at a given epoch, and this characteristic bending mass also increases with redshift – this has been attributed to a change in environments suppressing cold gas accretion with redshift and quenching (e.g., Dekel & Birnboim 2006; Daddi et al. 2022).

While optical and near-infrared (IR) light observed from the Earth is primarily sensitive to the stellar emission from galaxies at all redshifts (with the longer wavelengths being weighted to higher-redshift galaxies), far-IR light (from tens to around $1000\,\mu\mathrm{m}$; note that this also includes wavelengths often described as submillimetre at the longer end) is sensitive to the thermal emission from warm dust grains in galaxies at all redshifts. Since these dust grains are primarily produced by star-formation processes, there is a tight correlation between the far-IR luminosity (often defined as the integral of the luminosity density between 8 and $1000\,\mu\mathrm{m}$) and the SFR (e.g., Kennicutt 1998), and therefore a connection to the galaxy MS. It is therefore of interest to check the consistency between the SFRs derived from optical and near-IR photometry to those derived (independently) from far-IR photometry, and to see if there is evolution in the dust properties that can provide insight into the processes changing the MS.

There have been many large extragalactic surveys carried out by far-IR and submillimetre observatories, particularly by the *Herschel* Photodetector Array Camera and Spectrometer (PACS Poglitsch et al. 2010) at 70–$160\,\mu\mathrm{m}$, the *Herschel* Spectral and Photometric Imaging REceiver (SPIRE Griffin et al. 2010) at 250, 350, and $500\,\mu\mathrm{m}$, and the Submillimetre Common-User Bolometer Array 2 (SCUBA-2 Holland et al. 2013) at 450 and $850\,\mu\mathrm{m}$. *Herschel* effectively measures the peak of the thermal SEDs of most *Euclid* galaxies, providing effective constraints on dust temperatures (which is proportional to the peak frequency), while SCUBA-2 probes the Rayleigh–Jeans tail of the thermal SED, the amplitude of which is essentially proportional to dust mass. Moreover, *Herschel* has surveyed roughly $1000\,\mathrm{deg}^2$ of the extragalactic sky (and SCUBA-2 about $5\,\mathrm{deg}^2$), essentially all of which will ultimately overlap with *Euclid* by the final data release.

Compared to the exquisite angular resolution of *Euclid* (approximately 0″2), the angular resolution of *Herschel* and SCUBA-2 is much more coarse, ranging between about 10″ and 30″. Far-IR maps therefore do not individually detect most of the galaxies that *Euclid* sees, but rather blend these galaxies together into a coherent pattern that traces the large-scale structure. Making progress requires stacking, where the average value of the pixels at the locations of a large number of objects is calculated, as opposed to trying to directly measure the flux densities of each object in the map – more precisely, this operation calculates the covariance between a catalogue and a map (see e.g., Marsden et al. 2009; Wang et al. 2015). The *Herschel* properties of optical and near-IR catalogues have been investigated via stacking in other fields such as the UKIDSS Ultra-Deep Survey (UDS; Viero et al. 2013, 1 deg^2), the Cosmic Evolution Survey (COSMOS; Duivenvoorden et al. 2020, 2 deg^2), both UDS and COSMOS (Koprowski et al. 2024), and the Galaxy And Mass Assembly (GAMA) fields and the Stripe 82 region (Wang et al. 2016). However, the fields used in these studies are either small and suffer from sample variance to some degree, or the optical catalogues do not go beyond redshift 1. With *Euclid* we can dramatically expand these results to include millions of star-forming galaxies across tens of deg^2. Moreover, future *Euclid* data releases will continue to overlap with existing *Herschel* observations, eventually amounting to a billion galaxies over 1000 deg^2.

We therefore focus on stacking the entire Q1 catalogue on *Herschel* and SCUBA-2 maps, amounting to the largest study yet of this kind. In Sect. 2 we describe the *Euclid* catalogues and far-IR maps used in the analysis, in Sect. 3 we present our stacking pipeline, in Sect. 4 we show our results, and in Sect. 5 we discuss our findings. The paper concludes in Sect. 6. Throughout this paper we assume the cosmological parameters from Planck Collaboration VI (2020).

2. Data

The *Euclid* Q1 release is split into three fields: the EDF-F (12.1 deg^2); the EDF-N (22.9 deg^2); and the EDF-S (28.1 deg^2). Of these three fields, EDF-F and EDF-N have overlapping coverage from SPIRE. The SPIRE field overlapping with the EDF-F is known as 'CDFS-SWIRE', and the field overlapping with the EDF-N is known as the 'AKARI-NEP'. Here we describe the multiwavelength data in these two fields that we will be using.

2.1. Euclid catalogues and masks

The *Euclid* merging (MER) Q1 catalogue (Euclid Collaboration: Romelli et al. 2025) contains the photometry of all VIS- and NISP-detected galaxies, as well as ground-based photometry in the *u*, *g*, *r*, *i*, and *z* bands from various telescopes (see Tereno et al. in prep. for details). Here we make use of the *Euclid* catalogue described in Euclid Collaboration: Enia et al. (2025), which includes additional photometry from the Infrared Array Camera (IRAC) onboard the *Spitzer* Space Telescope (Fazio et al. 2004) at 3.6 and 4.5 μm. This catalogue also includes refitting of SEDs with the additional IRAC data in order to derive photometric redshifts, stellar masses, and SFRs. The final catalogue contains 2 884 906 objects in the EDF-F and 6 221 146 objects in the EDF-N. We note that this is somewhat fewer objects than in the full Q1 catalogue, since stars and other image artefacts were removed before cross-matching to IRAC.

Since in this study we are interested in the average properties of MS galaxies, we use the same colour cuts to remove quiescent galaxies. Specifically, galaxies are removed with NUV − r$^+$ > 3(r$^+$ − J) + 1 and NUV − r$^+$ > 3.1, leaving 1 318 898 objects in the EDF-F and 2 658 118 objects in the EDF-N.

In order to ensure an accurate stacking analysis, we need to take into account the fact that some regions within the *Euclid* footprint do not contain any extragalactic objects, due to contamination from bright stars. This can be done by calculating a mask that is associated with the *Euclid* catalogue, and propagating that mask through all the calculations.

For each of our far-IR images we therefore calculate the number of *Euclid* objects in each pixel, then lightly smooth the map using a Gaussian kernel. We then define the *Euclid* catalogue mask to be the regions where this smoothed map has a value less than a given threshold, determined visually by ensuring that the mask agreed well with the actual galaxy distribution. Defined this way, the *Euclid* mask removes far-IR pixels that have no extragalactic *Euclid* objects across a sufficiently large scale.

2.2. Far-IR imaging

The SPIRE maps of the EDF-F (or CDFS-SWIRE) and the EDF-N (or AKARI-NEP) were obtained from the *Herschel* Extragalactic Legacy Project (HELP) archive (Shirley et al. 2021).[1] The HELP data products include unfiltered maps and matched-filtered maps, along with their corresponding noise (or RMS) maps. Throughout this paper we use the unfiltered products because we do not expect these maps to have significant fluctuations caused by instrumental effects, nor significant contamination from dust in the Milky Way. The CDFS-SWIRE image covers 12.8 deg^2, while the AKARI-NEP image covers 9.0 deg^2 (although not all of this area overlaps with *Euclid*). The raw SPIRE data, RMS maps and masks for each of the two fields are shown in Figs. 1 and 2. In both maps extra observations were taken near the centres of the fields to decrease the noise and create small deep fields and wide shallow fields, and the HELP data products combine all of the observations into a single image.

In addition to SPIRE maps, the HELP archive also provides PACS maps at 100 and 160 μm, wherever the data were taken. For the EDF-F, the full area observed by SPIRE was also observed by PACS (albeit to a much shallower depth), which we make use of here. The AKARI-NEP was also observed, covering 0.6 deg^2 of the EDF-N. For these data only the output from the standard PACS processing pipeline is available; some filtering is done to the raw data in order to reduce strong 1/*f* noise and remove artefacts from bright sources, but the maps are not matched-filtered. The PACS data, RMS maps and masks are shown in Appendix A.

SCUBA-2 was used to map the AKARI-NEP (EDF-N) field as part of the SCUBA-2 Cosmology Legacy Survey (S2CLS; Geach et al. 2017), and this field was later expanded in the North Ecliptic Pole SCUBA-2 survey (NEPSC2; Shim et al. 2020).[2] The data products include unfiltered maps and matched-filtered maps, along with their corresponding RMS maps. As with the SPIRE images, here we use the unfiltered maps. The total area covered by SCUBA-2 in the AKARI-NEP is 2.9 deg^2, and the entirety of this field has been observed by *Euclid*. The SCUBA-2 data, RMS map and mask are shown alongside the PACS maps in Appendix A.

Despite the fact that we can down-weight noisy regions using RMS maps, very noisy pixels near the edges of these maps can still cause significant issues, since the uncertainties for re-

---

[1] https://hedam.lam.fr/HELP/
[2] https://dx.doi.org/10.5281/zenodo.3897405
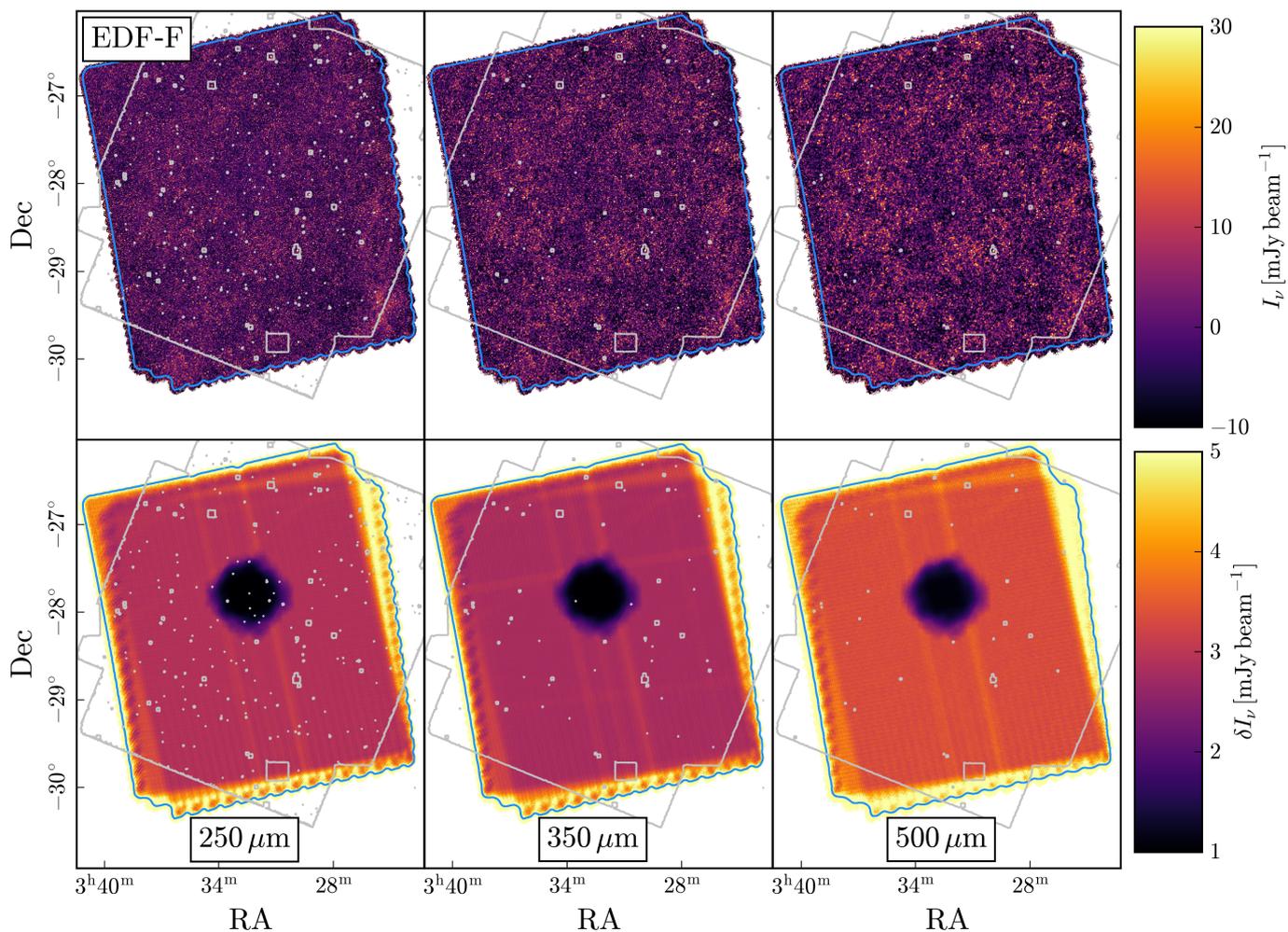
Fig. 1: *Top: Herschel*-SPIRE data covering the CDFS-SWIRE field (which overlaps with the EDF-F) at 250, 350, and 500 μm. The blue contour shows the mask applied to the SPIRE images in order to remove bad edge pixels. The grey contours show the corresponding *Euclid* catalogue mask, where masked rectangles are the locations of bright stars in the field that contaminate source extraction. *Bottom:* Same as the top panel, but showing the RMS of the *Herschel*-SPIRE data. Coordinates are conventional RA and Dec.

gions with few 'hits' can be underestimated. To mitigate this issue, we also create masks to remove problematic edge pixels. To make the mask for the SPIRE CDFS-SWIRE field we smooth the noise maps using a Gaussian kernel with a standard deviation of 7.5 pixels, then mask regions where the smoothed noise map has a value > 7 mJy beam^{-1}; for reference, typical noise values are < 4 mJy beam^{-1}. For the AKARI-NEP field this strategy does not work because the noise map is too inhomogeneous, so instead we manually define a rectangular masked region outside of which the noise pattern begins to deviate from the majority of the map. For the PACS maps of the CDFS-SWIRE field the noise is again quite inhomogeneous, so we also manually define a central region with a consistent noise level. For the PACS AKARI-NEP maps we smooth the noise maps using a Gaussian kernel with a standard deviation of 5 pixels and mask regions where the smoothed noise map has a value > 40 mJy beam^{-1} (compared to the typical noise level of about 30 mJy beam^{-1}). For the SCUBA-2 data, we simply mask pixels with noise values > 30 mJy beam^{-1} (compared to the typical noise level of about 10 mJy beam^{-1}). Lastly, the AKARI-NEP field contains NGC 6543 (the 'Cat's Eye Nebula'), which is particularly bright in the PACS and SCUBA-2 images. Since this is a Galactic object, we mask it before stacking our galaxy catalogue. These masks are also shown in Figs. 1, 2, A.1, and A.2 along with the *Euclid* catalogue masks.

2.3. Overlap between Euclid Q1 products and far-IR images

After accounting for the masked regions, the total overlapping area between the EDF-F and the SPIRE CDFS-SWIRE data is 10.8 deg^2, while for the EDF-N and the SPIRE AKARI-NEP data the total overlapping area is 6.8 deg^2, for a total area of 17.6 deg^2. Within the unmasked EDF-F region, the catalogue from Euclid Collaboration: Enia et al. (2025) contains about 1.5 million MS galaxies, while the EDF-N regions contains about 1.1 million galaxies (note that the exact values beyond the first digit depend somewhat on the SPIRE wavelength, since each SPIRE band has slightly different coverage). This brings the total number of MS galaxies overlapping with SPIRE to 2.6 million. For PACS, the total area available for stacking, after accounting for the *Euclid* mask, is 8.9 deg^2 in the EDF-F and 0.4 deg^2 in the EDF-N, with 1.3 million and 70 000 MS galaxies, respectively. The total PACS area is thus 9.3 deg^2, containing 1.4 million MS galaxies. For SCUBA-2, the total area available for
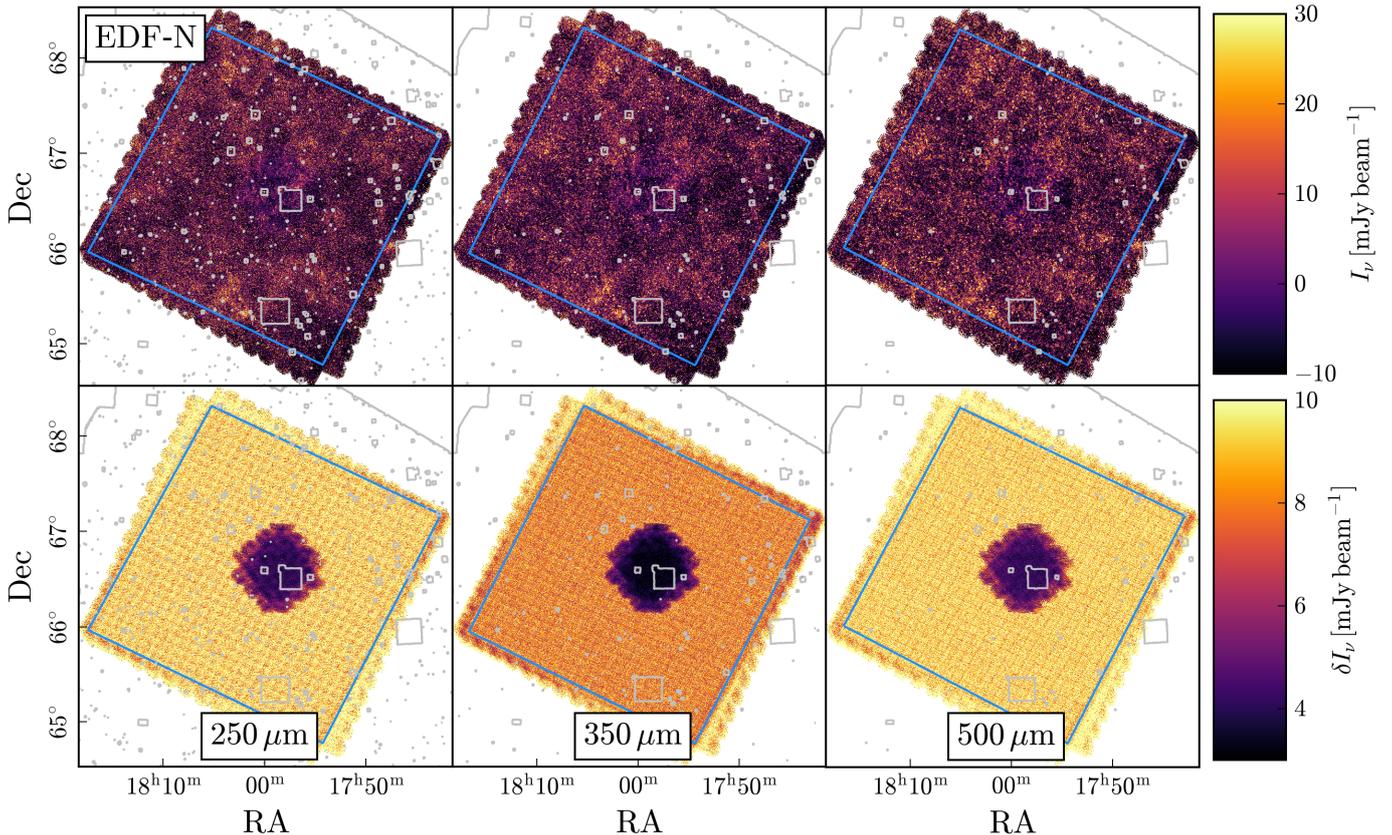
Fig. 2: Same as Fig. 1, but for the *Herschel*-SPIRE AKARI-NEP field (which overlaps with the EDF-N).

stacking (only in the EDF-N) is $2.4\,\mathrm{deg}^2$, and contains $240\,000$ galaxies.

3. Stacking method

3.1. Stacking algorithm

With a few small adjustments, we employ the stacking method called `SimStack` (Viero et al. 2013), which stacks on multiple catalogue bins simultaneously. The main advantage of `SimStack` is that it is not affected by galaxy clustering, since we do not need to assume that the galaxies we are stacking on are Poisson distributed. Briefly, after the input stacking catalogue is split into N bins, we solve for the N stacking amplitudes defined by the linear equation

$$y = S_1 X_1 + \cdots + S_N X_N \,, \tag{1}$$

where y is the data map being stacked on (in this case a *Herschel* or SCUBA-2 map at one wavelength), S_b are the average flux densities of the galaxies in bin b, and X_b are the beam-convolved images of the distribution of galaxies in the same bin. We note that in this analysis we subtract the noise-weighted mean from the data map y, and therefore we also subtract the noise-weighted means from each of the beam-convolved images X_b; this ensures that we do not need to worry about adding an arbitrary constant to our stacking model (see Viero et al. 2013). To construct the beam-convolved galaxy distribution images X_b we simply loop through the positions of all the galaxies in a given bin, adding a 1 to each pixel in the model image where a galaxy in bin b is located, then we convolve the image by the instrumental beam and subtract the weighted mean.

Equation (1) is a linear system and can thus be solved via the weighted least-squares method (see section 3.1 of Viero et al. 2013 for an explicit derivation). Moreover, we can use maps from multiple fields to fit for the stacked flux densities simultaneously. For M total pixels across all of the data maps, we define X as the $M \times N$ matrix where column i contains the beam-convolved images X_i and $\mathbf{y}$ is the $M \times 1$ vector of the data (note that X_i and y must be flattened from a 2D image to a 1D vector in the same way, and images from multiple fields must be added to the vectors and matrices in the same order). We also incorporate the weights (and the masks) in the diagonal $M \times M$ matrix W, where $W_{ii} = 1/\sigma_{ii}^2$ if the pixel is not masked, and otherwise `nan`. The best-fit stacking amplitudes are then just the solution to the weighted linear least-squares problem,

$$\hat{\mathbf{S}} = (\mathsf{X}^\mathsf{T} \mathsf{W} \mathsf{X})^{-1} \mathsf{X}^\mathsf{T} \mathsf{W} \mathbf{y} \,. \tag{2}$$

In traditional stacking, it is common to create small equally-sized cutouts around each source and average these cutouts together. Ideally, for far-IR images of unresolved galaxies, these should all look like the instrumental point-spread function (PSF), and so these 2D stacks are excellent tools for checking for systematic errors. We can easily generalise the 2D stacking method from regular stacking to `SimStack` by noting that while the central pixel in a regular 2D stack is the covariance between the map and the catalogue, the offset pixels represent the shifted cross-correlations. We can achieve the same result by calculating cross-correlations between our data y and our model $S_1 X_1 + \cdots + S_N X_N$. In practice, we offset the data images and corresponding weights by integer pixel values $(\Delta x, \Delta y)$ relative to the model image, then re-solve Eq. (2) for a new set of stacking flux densities $\hat{\mathbf{S}}$.

3.2. Stacking bins

To perform the stacking we define a set of N bins in stellar mass and redshift, produced from the *Euclid* catalogue. Euclid Collaboration: Enia et al. (2025) focused their study of the galaxy MS on galaxies with $0.2 < z < 3.0$, with the understanding that most catastrophic outliers have either mistakenly very low or very high redshifts. For a similar reason they also limited their sample to galaxies with $\log_{10}(M_*/M_\odot) \lesssim 11.5$, since the galaxies with larger stellar masses are likely to be outliers with very large redshifts. Finally, they estimated the stellar mass completeness of the sample as a function of redshift, finding $> 95\%$ completeness at the lowest redshift ($z = 0.2$) around $\log_{10}(M_*/M_\odot) \simeq 8$. We therefore split the *Euclid* catalogue into redshift bins between $z = 0.2$ and 3.0, with a spacing of $\Delta z = 0.2$, and into stellar mass bins between $\log_{10}(M_*/M_\odot) = 8.3$ and 11.5, with a spacing of $\Delta \log_{10}(M_*/M_\odot) = 0.4$.

We next add an additional layer to the stacking model that includes all of the remaining catalogued galaxies that do not fall into any redshift or stellar mass bin. We also include the quiescent galaxies in this additional bin. We finally add one more layer to the stacking model that takes into account the *Euclid* mask, which is necessary to reduce biases in the stack (see Duivenvoorden et al. 2020, for details). For this mask layer we invert the *Euclid* mask, convolve it with the instrumental beam, and then restore the masked pixels. This layer is intended to capture far-IR surface brightness leakage from near-IR galaxies that *Euclid* was unable to detect due to contamination from e.g., bright stars (although in practice this effect is small).

3.3. Instrumental beams

The final input required for stacking is a model of the *Herschel* and SCUBA-2 beams. For PACS, we use the model empirical beams provided by the HELP archive (Shirley et al. 2021). These were measured by stacking WISE-selected galaxies on the PACS maps and fitting an elliptical 2D Gaussian profile to the stack. The ellipticity is due to the fact that the PACS beam is not circularly-symmetric, and so for these data we use the best-fit beams for each PACS map separately.

For SPIRE, since the input maps are not filtered, we use the instrumental beams approximated as 2D Gaussians with full width at half maximum (FWHM) values of $18\rlap{.}''15$ at $250\,\mu m$, $25\rlap{.}''15$ at $350\,\mu m$, and $36\rlap{.}''3$ at $500\,\mu m$ (see Griffin et al. 2010). For the SCUBA-2 image, we use the updated beam profile from Mairs et al. (2021), which is the sum of two Gaussians. The first Gaussian (the main beam) has FWHM $= 11\rlap{.}''0$ and a relative amplitude of 0.98, while the second Gaussian (the error beam) has FWHM $= 49\rlap{.}''1$ and a relative amplitude of 0.02.

3.4. Estimating uncertainties

We estimate the uncertainties in the best-fit stack flux densities following Viero et al. (2013) by both propagating the weight matrix and by performing bootstrap resampling to determine the overlap between neighbouring bins. The statistical covariance matrix from solving the weighted linear least-squares system is analytic and can be calculated as

$$\Sigma_{\hat{S}} = (X^\mathsf{T} W X)^{-1} , \qquad (3)$$

and so the statistical uncertainty in $\hat{S}_i$ is just $\sqrt{\Sigma_{\hat{S},ii}}$. We add this in quadrature with the uncertainty from bootstrap resampling (which dominates the error budget); for this contribution,

we generate 100 random catalogues by drawing stellar masses and redshifts for each galaxy from their probability distributions. In principle the stellar masses and redshifts are correlated with each other and would require a full 2D posterior distribution for each galaxy, but we simplify the procedure by assuming that the distributions are Gaussian with a standard deviation equal to half the 68% confidence interval. We then rebin each random catalogue, re-solve Eq. (2), and calculate the standard deviation of the 100 random estimates of $\hat{S}$.

4. Results

4.1. Average far-IR flux densities of main-sequence Euclid galaxies

We ran our stacking algorithm (essentially `SimStack` generalised to provide 2D cross-correlations) on the *Herschel* and SCUBA-2 maps described in Sect. 2. We set the 2D stacking cutout size for each of the SPIRE wavelengths to be $200''$ (meaning that we solve Eq. 2 for offsets in a $200'' \times 200''$ grid), while for SCUBA-2 we set the cutout size to be $70''$ and for PACS we set the cutout size to be $40''$. The full 2D cross-correlations are shown in Appendix B. We find significant detections in most bins above $\log_{10}(M_*/M_\odot) = 10$, and the detections are generally consistent with the instrumental PSFs.

More precisely, for perfect point sources the 2D profile produced by our algorithm is the cross-correlation of the beam with itself; for a Gaussian, this increases the FWHM by a factor of $\sqrt{2}$. We tested this by computing the averaged 1D radial profiles of our 2D cross-correlations and comparing these to the expected PSF profiles. We find good agreement between the stacked signals and the PSFs for most bins with $\log_{10}(M_*/M_\odot) > 9.9$. Below this stellar mass we find that the 2D profiles can be more extended than the beam, with the largest effect seen at $500\,\mu m$ where the PSF is largest. This could be caused by a combination of the beam size and incompleteness in the *Euclid* catalogue; for example, dust galaxies bright at far-IR wavelengths are more likely to be undetected by *Euclid*, and these galaxies could have different clustering properties. However, as detailed in the following sections, we do not expect this extended emission to affect our results and so we do not attempt to correct for it.

As discussed previously, the central pixel values shown in the 2D stacks are the best-fit mean flux densities of the galaxies in the given bin (i.e., the covariances between the catalogue and the maps). For the high S/N detections, we checked that the central pixel in our 2D stacks is always the brightest pixel, meaning that there are no astrometric offsets between the *Euclid* catalogue and our stacking images. We provide these central values and the corresponding uncertainties in Appendix B.

4.2. Average SEDs of main-sequence Euclid galaxies

Our best-fit stacked flux densities contain information about the average far-IR SEDs of the *Euclid*-selected galaxies in each stellar mass and redshift bin. We model the lower frequencies of these SEDs using a standard modified blackbody for $\nu(1+z) < \nu_\alpha$ (which will be explained below):

$$S_\nu\,[\mathrm{mJy}] = A \left[\frac{\nu(1+z)}{\nu_0} \right]^\beta (1+z)\, B_{\nu(1+z)}(T_\mathrm{d}) \left[\frac{10^{29}\,\mathrm{mJy}}{\mathrm{W\,m^{-2}\,Hz^{-1}}} \right] , \quad (4)$$

where $B_\nu(T_\mathrm{d})$ is the blackbody function

$$B_\nu(T_\mathrm{d}) = \frac{2h\nu^3}{c^2} \frac{1}{e^{h\nu/kT_\mathrm{d}} - 1} . \qquad (5)$$

Since we are dealing with galaxies at $z < 3$, we ignore corrections related to the cosmic microwave background (CMB; see da Cunha et al. 2013). In these equations ν is the observed frequency, z is the redshift, h is the Planck constant, k is the Boltzmann constant, c is the speed of light, $T_{\rm d}$ is the dust temperature, and the factor of 10^{29} converts the observed flux density units from SI to mJy. The quantity ν_0 is not a free parameter of the model but sets the dust mass normalisation (as will be explained in Sect. 4.3), and we use $\nu_0 = 353\,$GHz. We note that this simple parameterization assumes the dust is optically thin and so we do not need to include the characteristic frequency where the optical depth is unity (e.g., Draine 2006; Drew & Casey 2022). This leaves the amplitude A, dust temperature T, and dust emissivity index β as the three free parameters.

At rest-frame mid-IR frequencies $\nu(1 + z) > \nu_\alpha$, i.e., around a few THz, the Wien side of the thermal SED falls off less steeply than an exponential, and is typically modelled as a power law with a slope of $-\alpha$ (e.g., Blain et al. 2003; Roseboom et al. 2013; Casey et al. 2014; Reuter et al. 2020). Since our PACS data cover this region of the SED, we need to include this phenomenological feature. To do so, we model the SED for $\nu(1 + z) > \nu_\alpha$ as

$$S_\nu\,[\text{mJy}] = A_\alpha \left[\frac{\nu(1+z)}{\nu_\alpha} \right]^{-\alpha} (1+z) \left[\frac{10^{29}\,\text{mJy}}{\text{W m}^{-2}\,\text{Hz}^{-1}} \right]. \tag{6}$$

Here A_α and ν_α are determined by matching the amplitude and slope of Eqs. (4) and (6). This gives $A_\alpha = A(\nu_\alpha/\nu_0)^\beta B_{\nu_\alpha}(T)$, and ν_α solves the equation $3 + \beta + \alpha = x e^x/(e^x - 1)$ where $x = h\nu_\alpha/kT$.

Since we do not have enough photometry information to constrain β on the Rayleigh–Jeans sides or α on the Wien sides of the SEDs, we fix these values to $\beta = 1.96$ and $\alpha = 2.3$ according to the mean values found for local far-IR-selected galaxies (Drew & Casey 2022). Fixing β and α to these values, we perform our SED fits on all redshift and stellar mass bins where all three SPIRE flux densities have been detected in the stack with S/N > 3, and if there is also a PACS detection at 100 or $160\,\mu$m with S/N > 3. The reason for these constraints is simply that we need the observed photometry to bracket the peak of the SED in order to properly constrain the dust temperature (which is directly proportional to the peak frequency). We include a 4% absolute calibration uncertainty and a 1.5% relative calibration uncertainty in the SPIRE bands, a 5% absolute calibration uncertainty in the PACS bands, and a 15% absolute calibration uncertainty in the SCUBA-2 band. The resulting best-fit SEDs are shown in Fig. 3, and the best-fit parameters are given in Appendix C. In this figure we do not show lowest stellar mass bins as we do not have enough far-IR photometry to fit SEDs. For two of the highest redshift and stellar mass bins, $z = 2.7$, $\log_{10}(M_*/M_\odot) = 10.9$ and 11.3, the fits provide unphysically high dust temperatures ($> 60\,$K), potentially due to contamination in the *Euclid* catalogue. We discard these two bins for the remainder of this work. As can be seen it is mainly the $\log_{10}(M_*/M_\odot) > 9.9$ bin where we have enough far-IR photometry to fit SEDs, and these bins show good agreement between the 2D cross-correlation profiles and the instrumental beams.

4.3. Derived parameters for main-sequence Euclid galaxies

From the best-fit parameters to Eq. (4) we can derive certain average physical properties for the galaxies in the *Euclid* catalogue. First, the best-fit temperatures $T_{\rm d}$ are already the rest-frame dust temperatures because we included the redshifts in the fits. Next, the best-fit amplitudes are directly proportional to the dust mass,

$M_{\rm d}$, and can be calculated using (e.g., Reuter et al. 2020; Eales & Ward 2024; Jolly et al. 2025)

$$M_{\rm d} = \frac{D_{\rm L}^2(z) A}{\kappa_0}, \tag{7}$$

where κ_0 is the calibration factor that scales the specific luminosity at the rest-frame frequency of ν_0 (the same reference frequency in our SED fit, see Eq. 4) to a dust mass and $D_{\rm L}$ is the luminosity distance. Here we use the factor $\kappa_0 = 0.077\,\text{m}^2\,\text{kg}^{-1}$, calibrated to the frequency $\nu_0 = 353\,$GHz (Dunne et al. 2000; da Cunha et al. 2008; Dunne et al. 2011), and we include an uncertainty of $\pm 0.02\,\text{m}^2\,\text{kg}^{-1}$ (from James et al. 2002). This approach uses the best-fit model to estimate the rest-frame specific luminosity at the frequency ν_0, as opposed to using a single measured flux density. There are many other values of κ_0 used throughout the literature, typically resulting in dust mass differences of a factor of a few; however, picking a different κ_0 only changes the absolute value of the dust mass, not any trends in stellar mass or redshift (although κ_0 could in principle vary with redshift). On the other hand, the dust emissivity index β can have an effect on the best-fit SEDs, and therefore any stellar mass and redshift trends. While we do not expect β to vary by much compared to the fiducial value of about 2, this could be investigated in future if more far-IR wavelengths could be added.

Lastly, we can estimate far-IR SFRs using the linear relation

$$\text{SFR}\,[\text{M}_\odot\,\text{yr}^{-1}] = 1.49 \times 10^{-10} L_{\rm FIR}\,[\text{L}_\odot] \tag{8}$$

(assuming a Kroupa initial mass function as done with the *Euclid* catalogue; see Euclid Collaboration: Tucci et al. 2025), where

$$L_{\rm FIR} = 4\pi D_{\rm L}^2(z) \left[\int_{\nu_1}^{\nu_\alpha} A \left(\frac{\nu}{\nu_0} \right)^\beta B_\nu(T_{\rm d})\,\text{d}\nu + \int_{\nu_\alpha}^{\nu_2} A_\alpha \left(\frac{\nu}{\nu_\alpha} \right)^{-\alpha}\,\text{d}\nu \right] \tag{9}$$

is the area under the far-IR SED between $\nu_1 = c/1000\,\mu$m and $\nu_2 = c/8\,\mu$m in the rest frame. Again we use $\beta = 1.96$ and $\alpha = 2.3$. We note that this derived physical parameter SFR is not independent of $T_{\rm d}$ and $M_{\rm d}$, but instead these three quantities are correlated.

In Appendix C we show the resulting physical parameters $T_{\rm d}$, $M_{\rm d}$, and SFR in each of the stellar mass and redshift bins where we have sufficient stacked photometry to derive these physical parameters, and we also provide the derived physical quantities. We find a clear trend of increasing dust temperature with redshift, and an increase in the dust mass from redshifts to around $z \simeq 2$. For the SFRs, we see an increase towards high-z, with a dependence on the stellar mass (as expected from the galaxy MS). These trends will be discussed further in Sect. 5.

4.4. The mean brightness of the CIB from stacking

We now turn to estimating the fraction of the CIB resolved by *Euclid*-selected galaxies in Q1. The average brightness of the extragalactic sky at far-IR wavelengths was measured by the Cosmic Background Explorer (COBE) satellite, which carried two relevant instruments: the Far Infrared Absolute Spectrophotometer (FIRAS; Mather et al. 1993); and the Diffuse Infrared Background Experiment (DIRBE; see Boggess et al. 1992). Analysis of these data provide the best available estimates of the absolute value of the surface brightness of the sky at far-IR wavelengths. *Herschel* and SCUBA-2, on the other hand, have no sensitivity to the monopole on the sky, but instead measure differences between sources and an unknown background, amounting to fluctuations caused by individual galaxies. The fraction of the CIB
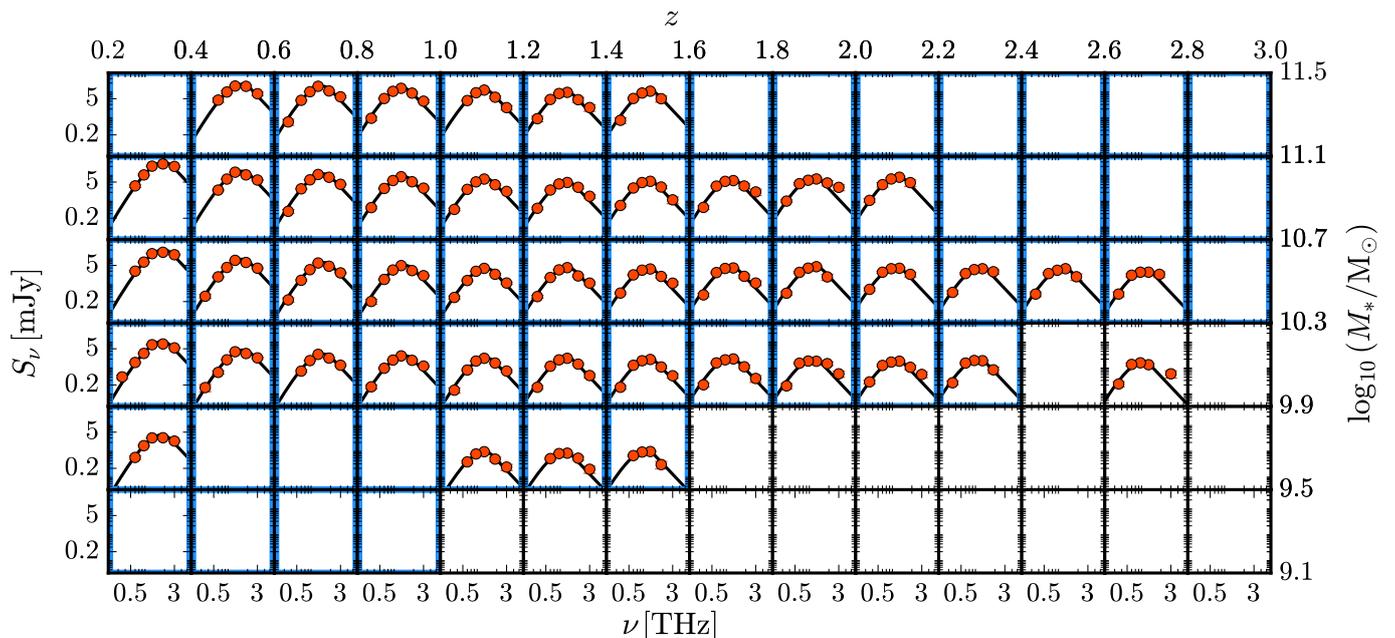
Fig. 3: Modified blackbody SEDs (with $\beta = 1.96$ and $\alpha = 2.3$) fit to the stacked *Herschel* and SCUBA-2 flux densities. The redshifts and stellar masses of each bin are indicated by the top and right axis labels, respectively. The best-fit parameters are given in Table C.1. SEDs have only been fit to bins where all three SPIRE flux densities are detected with S/N > 3, and at least one PACS flux density is detected with S/N > 3; panels are blank otherwise. Bins that are > 95% complete in stellar mass are highlighted in blue.

can be estimated by taking the sum of detected sources and dividing by the COBE-estimated background.

To do this, for each bin in the stack we multiply the mean flux density by the total number of SPIRE galaxies in the bin, then sum the contribution from all of the bins (including surface brightness leakage from the mask and the galaxies that do not fall in any redshift/stellar mass bin or are classified as quiescent). Finally, we divide this total flux density by the area of the SPIRE map after applying the masks (these are the areas given in Sect. 2.3). The results are shown in Table 1. We note that > 70% of our measured CIB surface brightness from star-forming galaxies comes from $\log_{10}(M_*/M_\odot) > 9.9$ bins which show good agreement between the 2D cross-correlation signals and the instrumental beams.

To determine the fraction of the CIB resolved by *Euclid*, we have to estimate the absolute value of the CIB measured by FIRAS and DIRBE. FIRAS measurements have been recalculated using an improved Galactic emission removal procedure at *Planck* wavelengths by Odegard et al. (2019), which should be more accurate than FIRAS alone at 350, 500, and 850 μm. From DIRBE, we use the results from a re-analysis of the data from the Cosmoglobe project (Watts et al. 2024), which provides measurements of the CIB intensity at 100, 140, and 240 μm. Additionally, Casandjian et al. (2024) used a combination of DIRBE and *Planck* data to estimate the CIB at 100, 140, 240, 350, 500, and 850 μm. Lastly we use the result from FIRAS alone at 250, 350, 500, and 850 μm by taking the best-fit spectral shape from (Fixsen et al. 1998); here the fit was done using a modified blackbody function, with $\beta = 0.64$ and $T = 18.5$ K. For the uncertainty we use the uncertainty in the best-fit amplitude. In order to correct the above 140 μm intensities to 160 μm, the 240 μm intensities to 250 μm, and the 550 μm intensities to 500 μm, we use this same best-fit spectral shape – these corrections range from 1 to 24%. All the CIB estimates are given in Table 1.

5. Discussion

5.1. Redshift trends of mean physical properties

In our stacking analysis we have found significant redshift trends for the dust temperatures, dust masses, and SFRs of average *Euclid*-selected galaxies. In order to interpret these results, we use the 95% stellar mass completeness limits from Euclid Collaboration: Enia et al. (2025) to select stacking bins that are > 95% complete; these bins are highlighted in blue in Fig. 3.

Focusing only on the stellar mass and redshift bins where the stellar masses are > 95% complete, we first compare our far-IR-derived SFRs to what is predicted from the star-forming MS. The *Euclid* SFRs were estimated by modelling solely optical and near-IR photometry from *Euclid* and its supporting observations, and the star-forming galaxies were split into four redshift bins between $z = 0.2$ and $z = 3.0$. In each bin the MS was parameterised as

$$\mathrm{SFR} = \frac{\mathrm{SFR_{max}}}{1 + (M_0/M_*)^\gamma},\tag{10}$$

with γ fixed to 1 and $\mathrm{SFR_{max}}$ and M_0 left as free parameters. Since our redshift bins are much smaller than what was used by Euclid Collaboration: Enia et al. (2025), we instead use the fit to Eq. (10) from Popesso et al. (2023), which was found to be in good agreement with the *Euclid* results. Popesso et al. (2023) also fixed $\gamma = 1$, letting $\log_{10}(\mathrm{SFR_{max}})(t) = a_0 + a_1 t$ and $\log_{10}(M_0)(t) = a_2 + a_3 t$. The resulting ratio of far-IR SFRs to the prediction from the MS are shown in Fig. 4. We note that below $\log_{10}(M_*/M_\odot) = 9.7$ we do not have any far-IR detections in the stellar mass-complete bins, so we only plot the results for the five most massive bins. We find good agreement between the two estimates, with a weighted mean ratio of 1.0 and a weighted standard deviation of 0.2.

Next, in Fig. 5 we show T_d versus time (bottom axis) and z (top axis), split by the different stellar mass bins used in our

Table 1: Contribution to the CIB from stacking the *Euclid* catalogue.

Band [μm]	Main gals. [Jy deg^{-2}]	Mask [Jy deg^{-2}]	Remaining gals. [Jy deg^{-2}]	**Total** [Jy deg^{-2}]	Fixsen [Jy deg^{-2}]	Odegard [Jy deg^{-2}]	Watts [Jy deg^{-2}]	Casandjian [Jy deg^{-2}]
100	34.3±1.1	0.088±0.035	32.8±0.6	**67.2 ± 1.3**	. . .	. . .	80±17	249±40
160	62.5±1.6	0.131±0.038	50.8±0.9	**113.4 ± 1.8**	. . .	. . .	158±106	271±86
250	101.0±0.7	0.621±0.004	78.2±0.1	**179.7 ± 0.7**	260±80	. . .	144±72	164±48
350	76.5±0.7	0.500±0.003	58.5±0.2	**135.5 ± 0.7**	200±61	175±10	. . .	114±11
500	42.8±0.7	0.340±0.003	35.2±0.2	**78.4 ± 0.7**	102±31	133±6	. . .	99±7
850	8.8±0.4	0.075±0.013	6.2±0.2	**15.0 ± 0.4**	43±13	45±5	. . .	35±4

Notes. The 'Main gals.' column is the value of the CIB from star-forming galaxies with reliable optical/near-IR SED fits, $8.3 < \log_{10}(M_*/M_\odot) < 11.5$, $0.2 < z < 3.0$, the 'Mask' column is the contribution to the CIB from the flux leakage through the *Euclid* mask, the 'Remaining gals.' column is the value of the CIB from galaxies outside this stellar mass and redshift range or classified as quiescent, and the 'Total' column (in bold) is the sum of these three contributions. The estimated absolute values of the CIB are in the right four columns, with references being Fixsen et al. (1998), Odegard et al. (2019), Watts et al. (2024), and Casandjian et al. (2024).
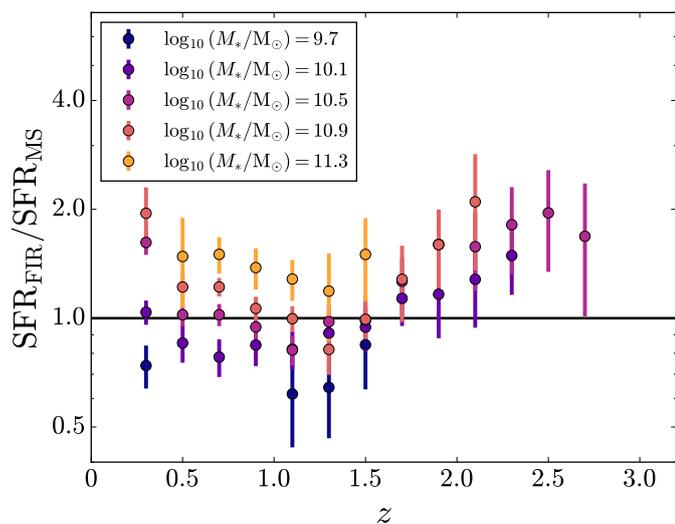
Fig. 4: Ratio of our SFRs measured from far-IR photometry to a parameterisation of the star-forming MS, shown as a function of redshift and split into different stellar mass stacking bins. Only redshift and stellar mass bins with > 95% completeness are shown. We use the MS parameterisation from Popesso et al. (2023), which a continuous function of z/t and is in good agreement with Euclid Collaboration: Enia et al. (2025).

stacking analysis. We find that average dust temperatures increase with redshift from about 20 to 35 K, without any obvious trend in stellar mass. Looking at the dust temperature trend plotted linearly as a function of time, we see that the data decrease steeply between 2 and 6 Gyr ($z = 3$ and 1), then plateau to a constant dust temperature until the present day. To capture this behaviour, we fit a phenomenological function of the form

$$T_{\rm d}(t) = T_2 + (T_1 - T_2)\, {\rm e}^{-t/\tau}\,, \tag{11}$$

where T_1 is the mean dust temperature of all star-forming galaxies at $t = 0$ Gyr, T_2 is the dust temperature all star-forming galaxies approach as t becomes large, and τ is the characteristic timescale. We find best-fit values of $T_1 = (79.7 \pm 7.4)$ K, $T_2 = (23.2 \pm 0.1)$ K, and $\tau = (1.6 \pm 0.1)$ Gyr.

For comparison, in Fig. 5 we also show a fit to the average dust temperature of star-forming galaxies as a function of redshift from Schreiber et al. (2017), which was later used to generate a simulated *Euclid* catalogue with far-IR photometry (see Sect. 5.3). Here a similar stacking analysis was used to estimate far-IR photometry in bins of redshift and stellar mass,

but as opposed to fitting a modified blackbody to the photometry (as done here), an empirical template was used to fit the data. They found that the dust temperatures increased linearly as a function of redshift, but as can be seen in Fig. 5 this approach appears to overestimate the dust temperatures relative to our analysis around $z \approx 1.5$. We also include the results from Koprowski et al. (2024), who stacked optically-selected catalogues on far-IR images and fit a modified blackbody to the photometry (with β and α fixed to the same values as used here); they found that the dust temperatures follow a quadratic polynomial in redshift, which we find agrees well with our exponential decay function. We note that neither of these studies found any trend in stellar mass. In Fig. 5 we also show the average dust temperature derived from a sample of local ($0.01 < z < 0.05$) star-forming galaxies from Lamperti et al. (2019). Since this sample includes bright galaxies, no stacking was required to estimate far-IR flux densities. SEDs were fit to the same modified blackbody function used here, although wavelengths $> 100\,\mu$m were not used in the fit so the transition to a power-law was not needed, and β was kept as a free parameter with best-fit values ranging from 1–2. After averaging over all of the dust temperatures in the sample, we find a mean value of 23.1 ± 0.1 K, consistent with our fit.

We next plot the dust mass, $M_{\rm d}$, and dust-to-stellar mass ratio, $M_{\rm d}/M_*$, in the same way for the same stellar-mass-complete bins. The results are shown in Fig. 6. Here we find an increase in dust mass (and the dust mass ratio) from $z = 0.2$ to around $z = 1$, followed by a plateau, for all stellar mass bins. We also find that the dust-to-stellar mass fraction decreases with increasing stellar mass at all redshifts.

These trends can be explained using our fit to Eq. (11) and the fit to Eq. (10) from Popesso et al. (2023), or indeed any fit to the MS that agrees with our far-IR-measured SFRs. By combining these two equations we can solve for the dust mass as a function of t (and therefore z). The resulting curves for the dust mass and dust-to-stellar mass ratio as a function of redshift are shown in Fig. 6 for each stellar mass bin – it is important to emphasise that these are not fits to the data, but predictions based on fits to the dust temperatures, SFRs, and stellar masses. We find an increase in dust mass and dust-to-stellar mass ratio up to $z = 1$; beyond this redshift, the curves predict a decrease in these quantities as opposed to a plateau; however, we note that the actual functional forms are very sensitive to the best-fit parameters to the dust temperature and SFR as a function of t and we do not have enough stacked photometry beyond $z = 1.5$ to properly constrain the model. We also see the same trend of decreasing dust-to-stellar mass fraction with increasing stellar
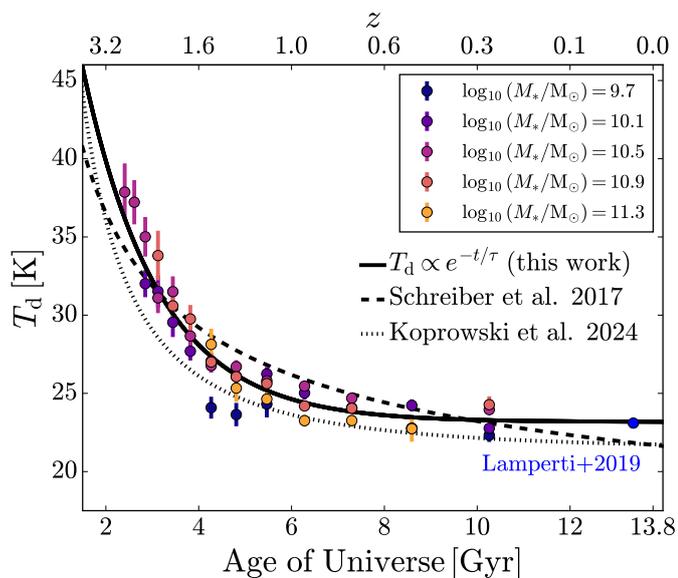
Fig. 5: Best-fit dust temperatures from our SED fitting, T_d, as a function of time (bottom axis) and redshift (top axis), considering only the redshift and stellar mass bins that are $>95\%$ complete. We show the dust temperature evolution for five different stellar mass bins, with the stellar mass values of the centres of the bins given in the legend. The solid curve is a fit to the simple form $T_2 + (T_1 - T_2)\, e^{-t/\tau}$, while the dotted line is the quadratic-in-redshift fit from Koprowski et al. (2024) and the dashed line is the linear-in-redshift fit from Schreiber et al. (2017). We also show published mean temperature estimates for star-forming galaxies at low redshift ($0.01 < z < 0.05$; Lamperti et al. 2019) in blue.

mass. The decrease in the-to-stellar mass ratio at redshifts <1 has been observed and discussed by Béthermin et al. (2015) as a consequence of decreasing SFRs which can no longer replenish metals becoming locked up in the existing stellar population. Similarly, more massive galaxies have lower sSFRs (SFR/M_*) and so they produce less dust per unit stellar mass, explaining the decrease in the dust-to-stellar mass fraction with stellar mass.

For comparison, we show the results from Millard et al. (2020) and Jolly et al. (2025). Both of these studies stacked on all optically-selected galaxies (i.e., including both star-forming and quiescent) as opposed to just star-forming galaxies as done here, and both only stacked on one far-IR band (SCUBA-2 850 μm for Millard et al. 2020, and ALMA 1.2 mm for Jolly et al. 2025). To convert the single far-IR photometry points to dust masses we used the same modified blackbody function fit to our data and our fit to the dust temperature as a function of t to scale the flux densities. The results are shown in the right panel of Fig. 6, where it can be seen that there is general agreement with our findings, although the dust mass-to-stellar mass ratios are lower at $z < 1.5$ likely due to the presence of quiescent galaxies in the comparison stacking catalogues. Interestingly, at higher redshifts ($z > 2$) where there is less contamination from quiescent galaxies, the stacked flux densities from Millard et al. (2020) suggest a plateauing mass ratio as opposed to a drop-off. This can be further investigated with future *Euclid* data releases once the deep fields get deeper, allowing us to probe higher redshifts with better statistical power.

The increasing dust temperatures with redshift have been attributed to the fact that MS galaxies have higher sSFRs at higher redshifts (e.g., Liang et al. 2019; Koprowski et al. 2024) and therefore contain more massive, young and hot stars. This can be seen in our stacking results in Fig. 7, where we plot the dust

temperature as a function of sSFR, separated by stellar mass in the same way as the previous plots. Galaxies with higher sS-FRs clearly tend to have higher dust temperatures, although the trend depends on stellar mass and redshift. To understand why, we note that we can predict the sSFR–T_d relation for each stellar mass and redshift bin by combining the star-forming MS (Eq. 11) and our fit to the dust temperature-t relation (Eq. 10). In Fig. 7 we show these predictions, where for each stellar mass bin we have calculated the relation between $z = 0.2$ (bottom-left of each curve) and $z = 3.0$ (top-right of each curve). Again, we emphasise that these are not fits to the data shown in the plot, but predictions based on other fits. At a given redshift the dust temperatures of all star-forming galaxies are independent of stellar mass, yet higher stellar mass galaxies have lower sSFRs (due to the bending of the MS), which leads to the mass dependence seen in Fig. 7.

One feature worth noting is that according to the star-forming MS, the SFRs (and sSFRs) of galaxies are continuously decreasing to zero as a function of time, yet the dust temperatures are not. Instead, the average dust temperatures appear to be converging to a constant value of about 23 K, independent of stellar mass. Indeed, it seems reasonable to expect that the dust temperatures of MS galaxies are not strictly proportional to the SFR/sSFR, since this would imply that galaxies with no star formation would have zero dust temperature, which is impossible. Instead, Eq. (11) implies that as the SFRs of galaxies fall below a certain threshold, the dust is no longer heated by hot young stars but by the existing cooler and older stellar population, which changes on timescales much longer than the current age of the Universe. Indeed, Chapman et al. (2003) showed that IRAS-selected galaxies are bi-modal in luminosity-versus-far-IR colour (a proxy for temperature) with a break around $10\,M_\odot\,\mathrm{yr}^{-1}$, and discussed a possible transition from cirrus-dominated SEDs to SFR-dominated SEDs.

5.2. Euclid's contribution to the CIB

Looking at the CIB estimates in Table 1, the latest estimates cannot be said to be in close agreement, and hence these CIB determinations are still dominated by systematic effects. This highlights the difficulty in subtracting zodiacal light and emission from the Milky Way, i.e., assessing the level of appropriate zero points when trying to determine the level of the extragalactic background. We can therefore only roughly estimate the fraction of the CIB resolved by the current Q1 *Euclid* catalogue: about 30–80% at 100 μm; 40–70% at 160 μm; 70–120% at 250 μm; 70–120% at 350 μm; 60–80% at 500 μm; and 30–40% at 850 μm.

A similar calculation was previously carried out using catalogues from the COSMOS field stacked on SPIRE images using the same stacking algorithm used here (Duivenvoorden et al. 2020); they found that r-band catalogues down to about magnitude 26 or K-band catalogues down to about magnitude 24 can recover essentially all of the CIB measured by FIRAS at all three SPIRE wavelengths. This provides a good benchmark for *Euclid* – the depth of the VIS images is about 24.7 in VIS and 23.2 in NISP, which approaches the depth of the COSMOS catalogues, and with a substantially larger numbers of catalogued objects.

In particular, at the SPIRE wavelengths we can say that we have recovered $>60\%$ of the CIB. These results are in line with Duivenvoorden et al. (2020), considering the r and K bands they used to create near-IR catalogues in their stacking study do not match perfectly with *Euclid*'s VIS and NISP instruments. It is reasonable to conclude that while we have not yet resolved the entire CIB with *Euclid* in Q1, $>60\%$ is consistent. As the Eu-
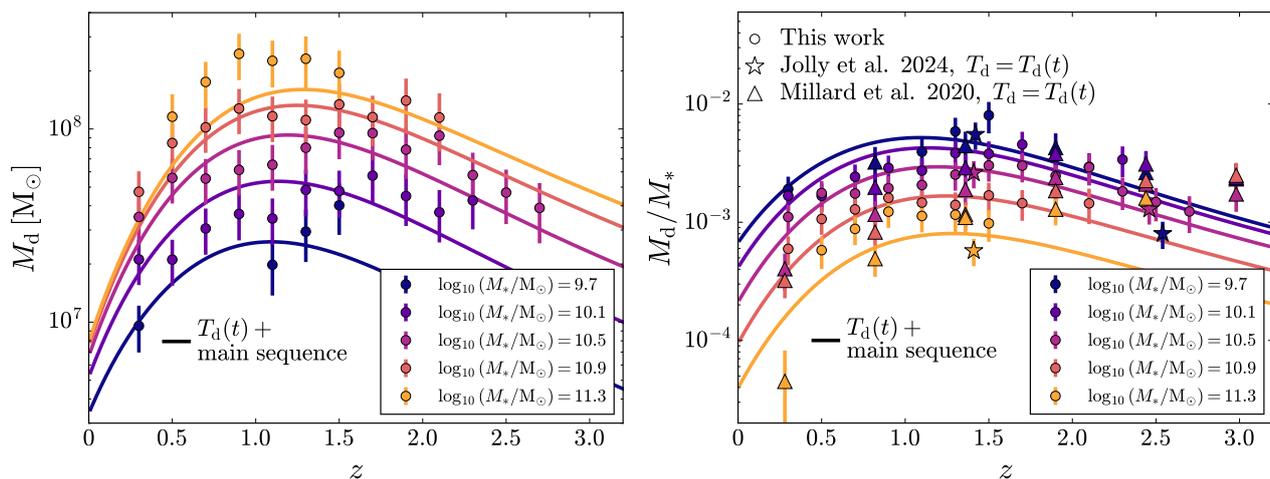
Fig. 6: *Left:* Best-fit dust masses from our SED fits, $M_{\rm d}$, as a function of redshift, considering only the redshift and stellar mass bins that are > 95% complete. *Right:* Same as the left panel but showing the best-fit dust mass-to-stellar mass ratio, where the stellar masses are from the *Euclid* catalogue and used to define the stacking bins. We also show SCUBA-2 stacking results from Millard et al. (2020), scaled to dust mass assuming the same modified blackbody SEDs used here and our best-fit dust temperature as a function of time, and ALMA 1.2 mm stacking results from Jolly et al. (2025) scaled in the same way. In both panels, the solid coloured curves show the predicted trends for the corresponding stellar masses by combining the star-forming MS from Popesso et al. (2023) with our fit to the dust temperature as a function of time.
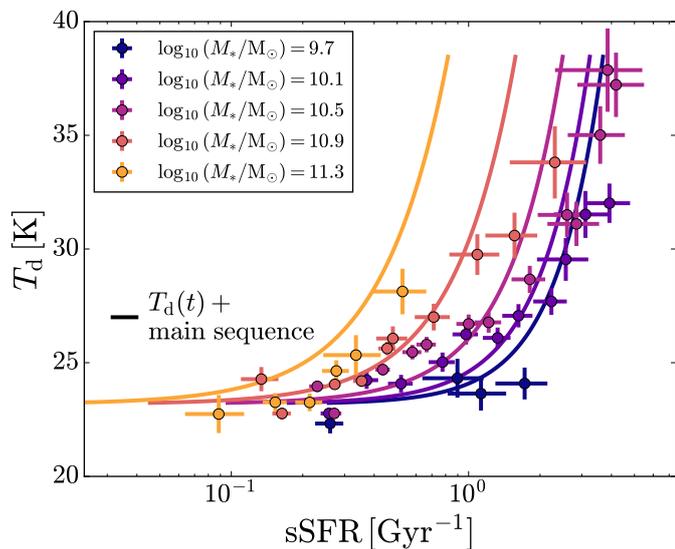
Fig. 7: Dust temperature as a function of sSFR from our best-fit far-IR SEDs, colour-coded to show the measured stellar mass dependence. Here we only show physical properties for bins that are > 95% complete. The coloured curves show the predicted trends for the corresponding stellar masses by combining the star-forming MS from Popesso et al. (2023) with our fit to the dust temperature as a function of time, ranging from $z = 0.2$ (starting at the bottom-left of each curve) to $z = 3.0$ (ending at the top-right of each curve).

clid Deep Fields get deeper, we can therefore expect to approach a more complete recovery of the CIB through *Euclid*-selected galaxies.

5.3. Comparison to the MAMBO simulation

A number of simulations able to reproduce *Euclid* observations have been investigated, including the MAMBO (Mocks with Abundance Matching in BOlogna; Girelli et al. 2020) mock catalogue. The MAMBO catalogue is based on the Millennium

Simulation (Springel et al. 2005) with physical properties prescribed using Empirical Galaxy Generator (EGG) code (Schreiber et al. 2017) across $3.14\,{\rm deg}^2$. In particular, magnitudes in the *Euclid* bands, as well as far-IR flux densities at the *Herschel* and SCUBA-2 bands used here, were calculated from the simulation by Euclid Collaboration: Parmar et al. (in prep.) and used to construct a mock *Euclid* catalogue at the depth of the Q1 catalogue (equal to the depth of the Euclid Wide Survey). Simulated stacked far-IR flux densities of star-forming MS galaxies were then calculated within the same redshift and stellar mass bins used here, from which we fit the same modified blackbody SEDs.

From this simulation we found slightly higher far-IR SFRs (although by a factor < 2) and dust masses (also larger by a factor < 2), with no significantly different redshift trends compared to our measurements. Interestingly, the simulated dust temperatures as a function of time are well-recovered by our pipeline, which we show in Fig. 8. The simulation does not show the same plateauing behaviour as with our measurements, but instead decrease monotonically with time across the entire redshift range investigated here. This difference can be attributed to details of EGG, which assigns dust temperatures using an equation linear in redshift (Eq. 14 in Schreiber et al. 2017) as opposed to quadratic in redshift, which better matches our observations.

5.4. Star-formation rate density

Lastly, we calculate the far-IR-derived SFR density (SFRD) as a function of redshift coming from the *Euclid* catalogue. We multiply the number of SPIRE stacking galaxies by the mean SFR, then sum the contributions from each stellar mass bin at a given redshift and divide by the volume of the redshift slice in the maps. Lastly, we average over every second redshift bin. In Fig. 9 we show the results for star-forming galaxies in purple, compared to several published estimates (Behroozi et al. 2013; Madau & Dickinson 2014; Koprowski et al. 2017). Since these literature curves include all galaxies (not just star-forming ones), we re-ran our stacking pipeline on the full *Euclid* catalogue using the same stellar mass and redshift bins, then re-fit the same SEDs

Fig. 8: Same as Fig. 5, but the data points are derived from fits to simulated stacked far-IR photometry in the MAMBO simulation (Euclid Collaboration: Parmar et al. in prep.).

Fig. 9: SFRD as a function of redshift for just star-forming galaxies (purple) and the full *Euclid* catalogue (green). The black curves show published SFRD fits from Koprowski et al. (2017), Behroozi et al. (2013), and Madau & Dickinson (2014), with the latter scaled by 0.63 to convert from Salpeter to Chabrier IMFs. Beyond redshift 1.5 our estimates of the SFRD are incomplete because we are not able to recover enough far-IR photometry to fit SEDs.

to derive the mean SFRs of all galaxies in each bin. We show the resulting SFRD for all *Euclid* galaxies as the green points.

What find that at $z < 1.5$ our total SFRD agrees well with the literature, but past this redshift our results are incomplete. This makes sense looking at Fig. 3, which shows that we are not able to recover enough far-IR photometry for high-stellar-mass galaxies at high redshifts to fit SEDs and derive SFRs. Future *Euclid* data releases will include more of these galaxies overlapping with more SPIRE data, allowing us to measure the complete SFRD past $z = 1.5$. These SFRD values should be regarded as lower bounds, since stacking only recovers the mean flux of cataloged galaxies and can miss contributions from galaxies that were not detected or heavily obscured galaxies.

6. Conclusions

We have stacked over 2 million star-forming galaxies from the *Euclid* Q1 catalogue across 17.6 deg^2 of far-IR imaging, providing robust statistics for their mean far-IR flux densities. We perform our stacking on *Herschel*-PACS 100- and 160-μm maps, *Herschel*-SPIRE 250-, 350-, and 500-μm maps, and SCUBA-2 850-μm maps. In order to avoid biases related to clustering, we use the `SimStack` algorithm, which simultaneously fits flux densities to far-IR beam-convolved model images of galaxy distributions in different bins.

Given the large number of galaxies available for stacking, we split the *Euclid* star-forming catalogue into eight stellar mass bins from $\log_{10}(M_*/M_\odot) = 8.3$ to $\log_{10}(M_*/M_\odot) = 11.5$, and 14 redshift bins from $z = 0.2$ to $z = 3.0$; beyond these ranges, the *Euclid* stellar masses and redshifts are no longer reliable. We find significant stacked detections in most bins at all wavelengths.

Using these average flux densities, we model the average far-IR SEDs of *Euclid* galaxies using a modified blackbody function transitioning to a power law at high frequencies, finding good fits where we are able to measure the stacked flux densities. From our fits we derive average dust temperatures, dust masses, and far-IR-derived SFRs, and we find significant redshift evolution in all of these parameters. In particular, we inves-

tigate the difference between our far-IR-derived SFRs and the SFRs predicted from the star-forming MS. We find consistent values between the two estimates, with no significant trend in redshift. The average dust temperature decreases as a function of time following a functional form $T_2 + (T_1 - T_2)\,\mathrm{e}^{-t/\tau}$, with no stellar mass dependence. We argue that the dust temperatures of MS galaxies below $z = 1$ have converged to a constant value ($T \simeq 23\,\mathrm{K}$) because the dust is now primarily heated by existing cooler and older stellar populations as opposed to hot young stars in star-forming regions. We also find that the average dust-to-stellar mass ratio increases for galaxies of all stellar mass up to $z \simeq 1$, and decreases with increasing stellar mass. This shows that the decreasing SFRs at low-z are no longer to replenish the dust reservoirs in galaxies, and similarly more massive galaxies have lower dust-to-stellar mass ratios due to their lower sSFRs compared to low mass galaxies. Lastly, we show that the correlation between dust temperature and SFR (and therefore sSFR) is stellar mass-dependent due to the fact that the dust temperatures are stellar mass-independent.

We compare our results to a recent mock *Euclid* catalogue with derived far-IR photometry, finding good agreement for the SFRs and dust masses. However, we show that the simulated catalogue predicts consistently decreasing dust temperatures below $z = 1$, in disagreement with our observation. We attribute this discrepancy to the model used to produce the dust temperatures, which assigns dust temperatures using a monotonically decreasing function of redshift as opposed to a functional form which converges to a constant value at low z.

In the future, *Euclid* will observe more area overlapping with far-IR surveys, and will obtain deeper VIS and NISP imaging in the Euclid Deep Fields, where some of the best existing far-IR and submillimetre imaging lies. These advances will provide even better statistics than are currently available, allowing our stacking analysis to extend to higher redshifts and lower stellar masses. In addition, upcoming far-IR facilities like the Cerro Chajnantor Atacama Telescope (CCAT-Prime Collaboration et al. 2023) will play an important role in better constraining

the Rayleigh–Jeans tail of the average far-IR SEDs, improving the SED constraints and derived physical parameters.

References

Behroozi, P. S., Wechsler, R. H., & Conroy, C. 2013, ApJ, 770, 57
Béthermin, M., Daddi, E., Magdis, G., et al. 2015, A&A, 573, A113
Blain, A. W., Barnard, V. E., & Chapman, S. C. 2003, MNRAS, 338, 733
Boggess, N. W., Mather, J. C., Weiss, R., et al. 1992, ApJ, 397, 420
Casandjian, J.-M., Ballet, J., & Grenier, I. 2024, ApJ, 969, 112
Casey, C. M., Narayanan, D., & Cooray, A. 2014, Phys. Rep., 541, 45
CCAT-Prime Collaboration, Aravena, M., Austermann, J. E., et al. 2023, ApJS, 264, 7
Chapman, S. C., Helou, G., Lewis, G. F., & Dale, D. A. 2003, ApJ, 588, 186
da Cunha, E., Charlot, S., & Elbaz, D. 2008, MNRAS, 388, 1595
da Cunha, E., Groves, B., Walter, F., et al. 2013, ApJ, 766, 13
Daddi, E., Delvecchio, I., Dimauro, P., et al. 2022, A&A, 661, L7
Dekel, A. & Birnboim, Y. 2006, MNRAS, 368, 2
Draine, B. T. 2006, ApJ, 636, 1114
Drew, P. M. & Casey, C. M. 2022, ApJ, 930, 142
Duivenvoorden, S., Oliver, S., Béthermin, M., et al. 2020, MNRAS, 491, 1355
Dunne, L., Eales, S., Edmunds, M., et al. 2000, MNRAS, 315, 115
Dunne, L., Gomez, H. L., da Cunha, E., et al. 2011, MNRAS, 417, 1510
Eales, S. & Ward, B. 2024, MNRAS, 529, 1130
Euclid Collaboration: Cropper, M., Al-Bahlawan, A., Amiaux, J., et al. 2025, A&A, 697, A2
Euclid Collaboration: Enia, A., Pozzetti, L., Bolzonella, M., et al. 2025, A&A, in press (Euclid Q1 SI), https://doi.org/10.1051/0004-6361/202554576, arXiv:2503.15314
Euclid Collaboration: Jahnke, K., Gillard, W., Schirmer, M., et al. 2025, A&A, 697, A3
Euclid Collaboration: Mellier, Y., Abdurro'uf, Acevedo Barroso, J., et al. 2025, A&A, 697, A1
Euclid Collaboration: Romelli, E., Kümmel, M., Dole, H., et al. 2025, A&A, in press (Euclid Q1 SI), https://doi.org/10.1051/0004-6361/202554586, arXiv:2503.15305
Euclid Collaboration: Tucci, M., Paltani, S., Hartley, W. G., et al. 2025, A&A, in press (Euclid Q1 SI), https://doi.org/10.1051/0004-6361/202554588, arXiv:2503.15306
Euclid Quick Release Q1. 2025, https://doi.org/10.57780/esa-2853f3b
Fazio, G. G., Hora, J. L., Allen, L. E., et al. 2004, ApJS, 154, 10
Fixsen, D. J., Dwek, E., Mather, J. C., Bennett, C. L., & Shafer, R. A. 1998, ApJ, 508, 123
Geach, J. E., Dunlop, J. S., Halpern, M., et al. 2017, MNRAS, 465, 1789
Girelli, G., Pozzetti, L., Bolzonella, M., et al. 2020, A&A, 634, A135
Griffin, M. J., Abergel, A., Abreu, A., et al. 2010, A&A, 518, L3
Holland, W. S., Bintley, D., Chapin, E. L., et al. 2013, MNRAS, 430, 2513
James, A., Dunne, L., Eales, S., & Edmunds, M. G. 2002, MNRAS, 335, 753
Jolly, J.-B., Knudsen, K., Laporte, N., et al. 2025, A&A, 693, A190
Kennicutt, Jr., R. C. 1998, ARA&A, 36, 189
Koprowski, M. P., Dunlop, J. S., Michałowski, M. J., et al. 2017, MNRAS, 471, 4155
Koprowski, M. P., Wijesekera, J. V., Dunlop, J. S., et al. 2024, A&A, 691, A164
Lamperti, I., Saintonge, A., De Looze, I., et al. 2019, MNRAS, 489, 4389
Liang, L., Feldmann, R., Kereš, D., et al. 2019, MNRAS, 489, 1397
Madau, P. & Dickinson, M. 2014, ARA&A, 52, 415
Mairs, S., Dempsey, J. T., Bell, G. S., et al. 2021, AJ, 162, 191
Marsden, G., Ade, P. A. R., Bock, J. J., et al. 2009, ApJ, 707, 1729
Mather, J. C., Fixsen, D. J., & Shafer, R. A. 1993, in SPIE Conf. Ser., Vol. 2019, Infrared Spaceborne Remote Sensing, ed. M. S. Scholl, 168–179
Millard, J. S., Eales, S. A., Smith, M. W. L., et al. 2020, MNRAS, 494, 293
Odegard, N., Weiland, J. L., Fixsen, D. J., et al. 2019, ApJ, 877, 40
Planck Collaboration VI. 2020, A&A, 641, A6
Poglitsch, A., Waelkens, C., Geis, N., et al. 2010, A&A, 518, L2
Popesso, P., Concas, A., Cresci, G., et al. 2023, MNRAS, 519, 1526
Reuter, C., Vieira, J. D., Spilker, J. S., et al. 2020, ApJ, 902, 78
Roseboom, I. G., Dunlop, J. S., Cirasuolo, M., et al. 2013, MNRAS, 436, 430
Schreiber, C., Elbaz, D., Pannella, M., et al. 2017, A&A, 602, A96
Shim, H., Kim, Y., Lee, D., et al. 2020, MNRAS, 498, 5065
Shirley, R., Duncan, K., Campos Varillas, M. C., et al. 2021, MNRAS, 507, 129
Speagle, J. S., Steinhardt, C. L., Capak, P. L., & Silverman, J. D. 2014, ApJS, 214, 15
Springel, V., White, S. D. M., Jenkins, A., et al. 2005, Nature, 435, 629
Viero, M. P., Moncelsi, L., Quadri, R. F., et al. 2013, ApJ, 779, 32
Wang, L., Norberg, P., Bethermin, M., et al. 2016, A&A, 592, L5
Wang, L., Viero, M., Ross, N. P., et al. 2015, MNRAS, 449, 4476
Watts, D. J., Galloway, M., Gjerløw, E., et al. 2024, arXiv e-prints, arXiv:2406.01491

[1] Department of Physics and Astronomy, University of British Columbia, Vancouver, BC V6T 1Z1, Canada
[2] Université de Strasbourg, CNRS, Observatoire astronomique de Strasbourg, UMR 7550, 67000 Strasbourg, France
[3] Herzberg Astronomy and Astrophysics Research Centre, 5071 W. Saanich Rd. Victoria, BC, V9E 2E7, Canada
[4] Department of Physics and Atmospheric Science, Dalhousie University, Halifax, NS, B3H 4R2, Canada
[5] Astrophysics Group, Blackett Laboratory, Imperial College London, London SW7 2AZ, UK
[6] School of Physics and Astronomy, Cardiff University, The Parade, Cardiff, CF24 3AA, UK
[7] INAF-Osservatorio di Astrofisica e Scienza dello Spazio di Bologna, Via Piero Gobetti 93/3, 40129 Bologna, Italy
[8] Dipartimento di Fisica e Astronomia, Università di Bologna, Via Gobetti 93/2, 40129 Bologna, Italy
[9] SRON Netherlands Institute for Space Research, Landleven 12, 9747 AD, Groningen, The Netherlands
[10] Kapteyn Astronomical Institute, University of Groningen, PO Box 800, 9700 AV Groningen, The Netherlands
[11] INAF-Osservatorio Astronomico di Brera, Via Brera 28, 20122 Milano, Italy
[12] IFPU, Institute for Fundamental Physics of the Universe, via Beirut 2, 34151 Trieste, Italy

[13] INAF-Osservatorio Astronomico di Trieste, Via G. B. Tiepolo 11, 34143 Trieste, Italy

[14] INFN, Sezione di Trieste, Via Valerio 2, 34127 Trieste TS, Italy

[15] SISSA, International School for Advanced Studies, Via Bonomea 265, 34136 Trieste TS, Italy

[16] INFN-Sezione di Bologna, Viale Berti Pichat 6/2, 40127 Bologna, Italy

[17] INAF-Osservatorio Astronomico di Padova, Via dell'Osservatorio 5, 35122 Padova, Italy

[18] Dipartimento di Fisica, Università di Genova, Via Dodecaneso 33, 16146, Genova, Italy

[19] INFN-Sezione di Genova, Via Dodecaneso 33, 16146, Genova, Italy

[20] Department of Physics "E. Pancini", University Federico II, Via Cinthia 6, 80126, Napoli, Italy

[21] INAF-Osservatorio Astronomico di Capodimonte, Via Moiariello 16, 80131 Napoli, Italy

[22] Dipartimento di Fisica, Università degli Studi di Torino, Via P. Giuria 1, 10125 Torino, Italy

[23] INFN-Sezione di Torino, Via P. Giuria 1, 10125 Torino, Italy

[24] INAF-Osservatorio Astrofisico di Torino, Via Osservatorio 20, 10025 Pino Torinese (TO), Italy

[25] European Space Agency/ESTEC, Keplerlaan 1, 2201 AZ Noordwijk, The Netherlands

[26] Leiden Observatory, Leiden University, Einsteinweg 55, 2333 CC Leiden, The Netherlands

[27] INAF-IASF Milano, Via Alfonso Corti 12, 20133 Milano, Italy

[28] Centro de Investigaciones Energéticas, Medioambientales y Tecnológicas (CIEMAT), Avenida Complutense 40, 28040 Madrid, Spain

[29] Port d'Informació Científica, Campus UAB, C. Albareda s/n, 08193 Bellaterra (Barcelona), Spain

[30] INAF-Osservatorio Astronomico di Roma, Via Frascati 33, 00078 Monteporzio Catone, Italy

[31] INFN section of Naples, Via Cinthia 6, 80126, Napoli, Italy

[32] Institute for Astronomy, University of Hawaii, 2680 Woodlawn Drive, Honolulu, HI 96822, USA

[33] Dipartimento di Fisica e Astronomia "Augusto Righi" - Alma Mater Studiorum Università di Bologna, Viale Berti Pichat 6/2, 40127 Bologna, Italy

[34] Instituto de Astrofísica de Canarias, Vía Láctea, 38205 La Laguna, Tenerife, Spain

[35] Institute for Astronomy, University of Edinburgh, Royal Observatory, Blackford Hill, Edinburgh EH9 3HJ, UK

[36] Jodrell Bank Centre for Astrophysics, Department of Physics and Astronomy, University of Manchester, Oxford Road, Manchester M13 9PL, UK

[37] European Space Agency/ESRIN, Largo Galileo Galilei 1, 00044 Frascati, Roma, Italy

[38] ESAC/ESA, Camino Bajo del Castillo, s/n., Urb. Villafranca del Castillo, 28692 Villanueva de la Cañada, Madrid, Spain

[39] Université Claude Bernard Lyon 1, CNRS/IN2P3, IP2I Lyon, UMR 5822, Villeurbanne, F-69100, France

[40] Aix-Marseille Université, CNRS, CNES, LAM, Marseille, France

[41] Institut de Ciències del Cosmos (ICCUB), Universitat de Barcelona (IEEC-UB), Martí i Franquès 1, 08028 Barcelona, Spain

[42] Institució Catalana de Recerca i Estudis Avançats (ICREA), Passeig de Lluís Companys 23, 08010 Barcelona, Spain

[43] Institut de Ciencies de l'Espai (IEEC-CSIC), Campus UAB, Carrer de Can Magrans, s/n Cerdanyola del Vallés, 08193 Barcelona, Spain

[44] UCB Lyon 1, CNRS/IN2P3, IUF, IP2I Lyon, 4 rue Enrico Fermi, 69622 Villeurbanne, France

[45] Mullard Space Science Laboratory, University College London, Holmbury St Mary, Dorking, Surrey RH5 6NT, UK

[46] Departamento de Física, Faculdade de Ciências, Universidade de Lisboa, Edifício C8, Campo Grande, PT1749-016 Lisboa, Portugal

[47] Instituto de Astrofísica e Ciências do Espaço, Faculdade de Ciências, Universidade de Lisboa, Campo Grande, 1749-016 Lisboa, Portugal

[48] Department of Astronomy, University of Geneva, ch. d'Ecogia 16, 1290 Versoix, Switzerland

[49] Université Paris-Saclay, CNRS, Institut d'astrophysique spatiale, 91405, Orsay, France

[50] INFN-Padova, Via Marzolo 8, 35131 Padova, Italy

[51] Aix-Marseille Université, CNRS/IN2P3, CPPM, Marseille, France

[52] INAF-Istituto di Astrofisica e Planetologia Spaziali, via del Fosso del Cavaliere, 100, 00100 Roma, Italy

[53] Space Science Data Center, Italian Space Agency, via del Politecnico snc, 00133 Roma, Italy

[54] INFN-Bologna, Via Irnerio 46, 40126 Bologna, Italy

[55] University Observatory, LMU Faculty of Physics, Scheinerstrasse 1, 81679 Munich, Germany

[56] Max Planck Institute for Extraterrestrial Physics, Giessenbachstr. 1, 85748 Garching, Germany

[57] Universitäts-Sternwarte München, Fakultät für Physik, Ludwig-Maximilians-Universität München, Scheinerstrasse 1, 81679 München, Germany

[58] Institute of Theoretical Astrophysics, University of Oslo, P.O. Box 1029 Blindern, 0315 Oslo, Norway

[59] Jet Propulsion Laboratory, California Institute of Technology, 4800 Oak Grove Drive, Pasadena, CA, 91109, USA

[60] Department of Physics, Lancaster University, Lancaster, LA1 4YB, UK

[61] Felix Hormuth Engineering, Goethestr. 17, 69181 Leimen, Germany

[62] Technical University of Denmark, Elektrovej 327, 2800 Kgs. Lyngby, Denmark

[63] Cosmic Dawn Center (DAWN), Denmark

[64] Max-Planck-Institut für Astronomie, Königstuhl 17, 69117 Heidelberg, Germany

[65] NASA Goddard Space Flight Center, Greenbelt, MD 20771, USA

[66] Department of Physics and Astronomy, University College London, Gower Street, London WC1E 6BT, UK

[67] Department of Physics and Helsinki Institute of Physics, Gustaf Hällströmin katu 2, University of Helsinki, 00014 Helsinki, Finland

[68] Université de Genève, Département de Physique Théorique and Centre for Astroparticle Physics, 24 quai Ernest-Ansermet, CH-1211 Genève 4, Switzerland

[69] Department of Physics, P.O. Box 64, University of Helsinki, 00014 Helsinki, Finland

[70] Helsinki Institute of Physics, Gustaf Hällströmin katu 2, University of Helsinki, 00014 Helsinki, Finland

[71] Laboratoire d'etude de l'Univers et des phenomenes eXtremes, Observatoire de Paris, Université PSL, Sorbonne Université, CNRS, 92190 Meudon, France

[72] SKAO, Jodrell Bank, Lower Withington, Macclesfield SK11 9FT, United Kingdom

[73] Centre de Calcul de l'IN2P3/CNRS, 21 avenue Pierre de Coubertin 69627 Villeurbanne Cedex, France

[74] Dipartimento di Fisica "Aldo Pontremoli", Università degli Studi di Milano, Via Celoria 16, 20133 Milano, Italy

[75] INFN-Sezione di Milano, Via Celoria 16, 20133 Milano, Italy

[76] University of Applied Sciences and Arts of Northwestern Switzerland, School of Computer Science, 5210 Windisch, Switzerland

[77] Universität Bonn, Argelander-Institut für Astronomie, Auf dem Hügel 71, 53121 Bonn, Germany

[78] INFN-Sezione di Roma, Piazzale Aldo Moro, 2 - c/o Dipartimento di Fisica, Edificio G. Marconi, 00185 Roma, Italy

[79] Dipartimento di Fisica e Astronomia "Augusto Righi" - Alma Mater Studiorum Università di Bologna, via Piero Gobetti 93/2, 40129 Bologna, Italy

[80] Department of Physics, Institute for Computational Cosmology, Durham University, South Road, Durham, DH1 3LE, UK

[81] Université Paris Cité, CNRS, Astroparticule et Cosmologie, 75013 Paris, France

[82] CNRS-UCB International Research Laboratory, Centre Pierre Binétruy, IRL2007, CPB-IN2P3, Berkeley, USA

[83] University of Applied Sciences and Arts of Northwestern Switzerland, School of Engineering, 5210 Windisch, Switzerland

[84] Institut d'Astrophysique de Paris, 98bis Boulevard Arago, 75014, Paris, France

[85] Institut d'Astrophysique de Paris, UMR 7095, CNRS, and Sorbonne Université, 98 bis boulevard Arago, 75014 Paris, France

[86] Institute of Physics, Laboratory of Astrophysics, Ecole Polytechnique Fédérale de Lausanne (EPFL), Observatoire de Sauverny, 1290 Versoix, Switzerland

[87] Telespazio UK S.L. for European Space Agency (ESA), Camino bajo del Castillo, s/n, Urbanizacion Villafranca del Castillo, Villanueva de la Cañada, 28692 Madrid, Spain

[88] Institut de Física d'Altes Energies (IFAE), The Barcelona Institute of Science and Technology, Campus UAB, 08193 Bellaterra (Barcelona), Spain

[89] DARK, Niels Bohr Institute, University of Copenhagen, Jagtvej 155, 2200 Copenhagen, Denmark

[90] Waterloo Centre for Astrophysics, University of Waterloo, Waterloo, Ontario N2L 3G1, Canada

[91] Department of Physics and Astronomy, University of Waterloo, Waterloo, Ontario N2L 3G1, Canada

[92] Perimeter Institute for Theoretical Physics, Waterloo, Ontario N2L 2Y5, Canada

[93] Université Paris-Saclay, Université Paris Cité, CEA, CNRS, AIM, 91191, Gif-sur-Yvette, France

[94] Centre National d'Etudes Spatiales – Centre spatial de Toulouse, 18 avenue Edouard Belin, 31401 Toulouse Cedex 9, France

[95] Institute of Space Science, Str. Atomistilor, nr. 409 Măgurele, Ilfov, 077125, Romania

[96] Consejo Superior de Investigaciones Cientificas, Calle Serrano 117, 28006 Madrid, Spain

[97] Universidad de La Laguna, Departamento de Astrofísica, 38206 La Laguna, Tenerife, Spain

[98] Dipartimento di Fisica e Astronomia "G. Galilei", Università di Padova, Via Marzolo 8, 35131 Padova, Italy

[99] Institut für Theoretische Physik, University of Heidelberg, Philosophenweg 16, 69120 Heidelberg, Germany

[100] Institut de Recherche en Astrophysique et Planétologie (IRAP), Université de Toulouse, CNRS, UPS, CNES, 14 Av. Edouard Belin, 31400 Toulouse, France

[101] Université St Joseph; Faculty of Sciences, Beirut, Lebanon

[102] Departamento de Física, FCFM, Universidad de Chile, Blanco Encalada 2008, Santiago, Chile

[103] Universität Innsbruck, Institut für Astro- und Teilchenphysik, Technikerstr. 25/8, 6020 Innsbruck, Austria

[104] Institut d'Estudis Espacials de Catalunya (IEEC), Edifici RDIT, Campus UPC, 08860 Castelldefels, Barcelona, Spain

[105] Satlantis, University Science Park, Sede Bld 48940, Leioa-Bilbao, Spain

[106] Institute of Space Sciences (ICE, CSIC), Campus UAB, Carrer de Can Magrans, s/n, 08193 Barcelona, Spain

[107] Infrared Processing and Analysis Center, California Institute of Technology, Pasadena, CA 91125, USA

[108] Instituto de Astrofísica e Ciências do Espaço, Faculdade de Ciências, Universidade de Lisboa, Tapada da Ajuda, 1349-018 Lisboa, Portugal

[109] Cosmic Dawn Center (DAWN)

[110] Niels Bohr Institute, University of Copenhagen, Jagtvej 128, 2200 Copenhagen, Denmark

[111] Universidad Politécnica de Cartagena, Departamento de Electrónica y Tecnología de Computadoras, Plaza del Hospital 1, 30202 Cartagena, Spain

[112] Astronomisches Rechen-Institut, Zentrum für Astronomie der Universität Heidelberg, Mönchhofstr. 12-14, 69120 Heidelberg, Germany

[113] Dipartimento di Fisica e Scienze della Terra, Università degli Studi di Ferrara, Via Giuseppe Saragat 1, 44122 Ferrara, Italy

[114] Istituto Nazionale di Fisica Nucleare, Sezione di Ferrara, Via Giuseppe Saragat 1, 44122 Ferrara, Italy

[115] INAF, Istituto di Radioastronomia, Via Piero Gobetti 101, 40129 Bologna, Italy

[116] Astronomical Observatory of the Autonomous Region of the Aosta Valley (OAVdA), Loc. Lignan 39, I-11020, Nus (Aosta Valley), Italy

[117] Université Côte d'Azur, Observatoire de la Côte d'Azur, CNRS, Laboratoire Lagrange, Bd de l'Observatoire, CS 34229, 06304 Nice cedex 4, France

[118] Department of Physics, Oxford University, Keble Road, Oxford OX1 3RH, UK

[119] Instituto de Astrofísica de Canarias (IAC); Departamento de Astrofísica, Universidad de La Laguna (ULL), 38200, La Laguna, Tenerife, Spain

[120] Université PSL, Observatoire de Paris, Sorbonne Université, CNRS, LERMA, 75014, Paris, France

[121] Université Paris-Cité, 5 Rue Thomas Mann, 75013, Paris, France

[122] Dipartimento di Fisica, Sapienza Università di Roma, Piazzale Aldo Moro 2, 00185 Roma, Italy

[123] Aurora Technology for European Space Agency (ESA), Camino bajo del Castillo, s/n, Urbanizacion Villafranca del Castillo, Villanueva de la Cañada, 28692 Madrid, Spain

[124] ICL, Junia, Université Catholique de Lille, LITL, 59000 Lille, France

[125] ICSC - Centro Nazionale di Ricerca in High Performance Computing, Big Data e Quantum Computing, Via Magnanelli 2, Bologna, Italy

[126] Instituto de Física Teórica UAM-CSIC, Campus de Cantoblanco, 28049 Madrid, Spain

[127] CERCA/ISO, Department of Physics, Case Western Reserve University, 10900 Euclid Avenue, Cleveland, OH 44106, USA

[128] Technical University of Munich, TUM School of Natural Sciences, Physics Department, James-Franck-Str. 1, 85748 Garching, Germany

[129] Max-Planck-Institut für Astrophysik, Karl-Schwarzschild-Str. 1, 85748 Garching, Germany

[130] Laboratoire Univers et Théorie, Observatoire de Paris, Université PSL, Université Paris Cité, CNRS, 92190 Meudon, France

[131] Departamento de Física Fundamental. Universidad de Salamanca. Plaza de la Merced s/n. 37008 Salamanca, Spain

[132] Center for Data-Driven Discovery, Kavli IPMU (WPI), UTIAS, The University of Tokyo, Kashiwa, Chiba 277-8583, Japan

[133] Ludwig-Maximilians-University, Schellingstrasse 4, 80799 Munich, Germany

[134] Max-Planck-Institut für Physik, Boltzmannstr. 8, 85748 Garching, Germany

[135] Dipartimento di Fisica - Sezione di Astronomia, Università di Trieste, Via Tiepolo 11, 34131 Trieste, Italy

[136] California Institute of Technology, 1200 E California Blvd, Pasadena, CA 91125, USA

[137] Department of Physics & Astronomy, University of California Irvine, Irvine CA 92697, USA

[138] Department of Mathematics and Physics E. De Giorgi, University of Salento, Via per Arnesano, CP-I93, 73100, Lecce, Italy

[139] INFN, Sezione di Lecce, Via per Arnesano, CP-193, 73100, Lecce, Italy

[140] INAF-Sezione di Lecce, c/o Dipartimento Matematica e Fisica, Via per Arnesano, 73100, Lecce, Italy

[141] Departamento Física Aplicada, Universidad Politécnica de Cartagena, Campus Muralla del Mar, 30202 Cartagena, Murcia, Spain

[142] Instituto de Física de Cantabria, Edificio Juan Jordá, Avenida de los Castros, 39005 Santander, Spain

[143] CEA Saclay, DFR/IRFU, Service d'Astrophysique, Bat. 709, 91191 Gif-sur-Yvette, France

[144] Institute of Cosmology and Gravitation, University of Portsmouth, Portsmouth PO1 3FX, UK

[145] Department of Astronomy, University of Florida, Bryant Space Science Center, Gainesville, FL 32611, USA

[146] Department of Computer Science, Aalto University, PO Box 15400, Espoo, FI-00 076, Finland

[147] Instituto de Astrofísica de Canarias, c/ Via Lactea s/n, La Laguna 38200, Spain. Departamento de Astrofísica de la Universidad de La Laguna, Avda. Francisco Sanchez, La Laguna, 38200, Spain

[148] Caltech/IPAC, 1200 E. California Blvd., Pasadena, CA 91125, USA

[149] Ruhr University Bochum, Faculty of Physics and Astronomy, Astronomical Institute (AIRUB), German Centre for Cosmological Lensing (GCCL), 44780 Bochum, Germany

[150] Department of Physics and Astronomy, Vesilinnantie 5, University of Turku, 20014 Turku, Finland

[151] Serco for European Space Agency (ESA), Camino bajo del Castillo, s/n, Urbanizacion Villafranca del Castillo, Villanueva de la Cañada, 28692 Madrid, Spain

[152] ARC Centre of Excellence for Dark Matter Particle Physics, Melbourne, Australia

[153] Centre for Astrophysics & Supercomputing, Swinburne University of Technology, Hawthorn, Victoria 3122, Australia

[154] Department of Physics and Astronomy, University of the Western Cape, Bellville, Cape Town, 7535, South Africa

[155] DAMTP, Centre for Mathematical Sciences, Wilberforce Road, Cambridge CB3 0WA, UK

[156] Kavli Institute for Cosmology Cambridge, Madingley Road, Cambridge, CB3 0HA, UK

[157] Department of Astrophysics, University of Zurich, Winterthurerstrasse 190, 8057 Zurich, Switzerland

[158] Department of Physics, Centre for Extragalactic Astronomy, Durham University, South Road, Durham, DH1 3LE, UK

[159] Institute for Theoretical Particle Physics and Cosmology (TTK), RWTH Aachen University, 52056 Aachen, Germany

[160] IRFU, CEA, Université Paris-Saclay 91191 Gif-sur-Yvette Cedex, France

[161] Oskar Klein Centre for Cosmoparticle Physics, Department of Physics, Stockholm University, Stockholm, SE-106 91, Sweden

[162] Univ. Grenoble Alpes, CNRS, Grenoble INP, LPSC-IN2P3, 53, Avenue des Martyrs, 38000, Grenoble, France

[163] INAF-Osservatorio Astrofisico di Arcetri, Largo E. Fermi 5, 50125, Firenze, Italy

[164] Centro de Astrofísica da Universidade do Porto, Rua das Estrelas, 4150-762 Porto, Portugal

[165] Instituto de Astrofísica e Ciências do Espaço, Universidade do Porto, CAUP, Rua das Estrelas, PT4150-762 Porto, Portugal

[166] HE Space for European Space Agency (ESA), Camino bajo del Castillo, s/n, Urbanizacion Villafranca del Castillo, Villanueva de la Cañada, 28692 Madrid, Spain

[167] INAF - Osservatorio Astronomico d'Abruzzo, Via Maggini, 64100, Teramo, Italy

[168] Theoretical astrophysics, Department of Physics and Astronomy, Uppsala University, Box 516, 751 37 Uppsala, Sweden

[169] Mathematical Institute, University of Leiden, Einsteinweg 55, 2333 CA Leiden, The Netherlands

[170] Institute of Astronomy, University of Cambridge, Madingley Road, Cambridge CB3 0HA, UK

[171] Univ. Lille, CNRS, Centrale Lille, UMR 9189 CRIStAL, 59000 Lille, France

[172] Department of Physics and Astronomy, University of California, Davis, CA 95616, USA

[173] Department of Astrophysical Sciences, Peyton Hall, Princeton University, Princeton, NJ 08544, USA

[174] Space physics and astronomy research unit, University of Oulu, Pentti Kaiteran katu 1, FI-90014 Oulu, Finland

[175] Center for Computational Astrophysics, Flatiron Institute, 162 5th Avenue, 10010, New York, NY, USA

Appendix A: PACS and SCUBA-2 field overviews

In Fig. A.1 we show the *Herschel*-PACS 100- and 160-μm data and RMS maps overlapping with the EDF-F and EDF-N. We also show the SCUBA-2 data and RMS map overlapping with the EDF-N in Fig. A.2. In both figures the *Euclid* mask is shown as the grey contours. The bright resolved source in the EDF-N is NGC 6543 (the 'Cat's Eye Nebula'), which we mask prior to the stacking.
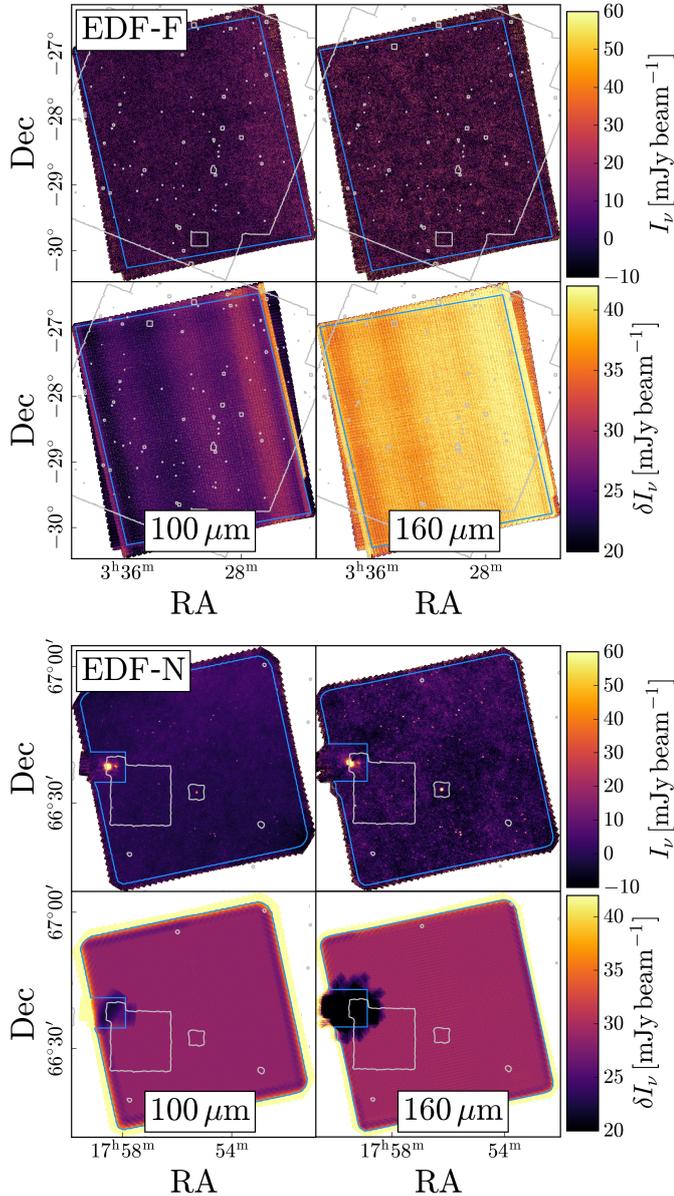
Fig. A.1: *Top:* Same as Fig. 1, but for the PACS observations of the CDFS-SWIRE (EDF-F) field. *Bottom:* Same as the above panel, but for the PACS observations of the AKARI-NEP (EDF-N) field.

Appendix B: Stacking cutouts and flux densities

Here we show the 2D cross-correlations from our stacking algorithm and provide a table of stacked flux densities. The 2D stacking results for the star-forming galaxies in the *Euclid* catalogue are shown in Fig. B.1 (for SPIRE), Fig. B.2 (for PACS), and Fig. B.3 (for SCUBA-2). We show both the signal (in units of
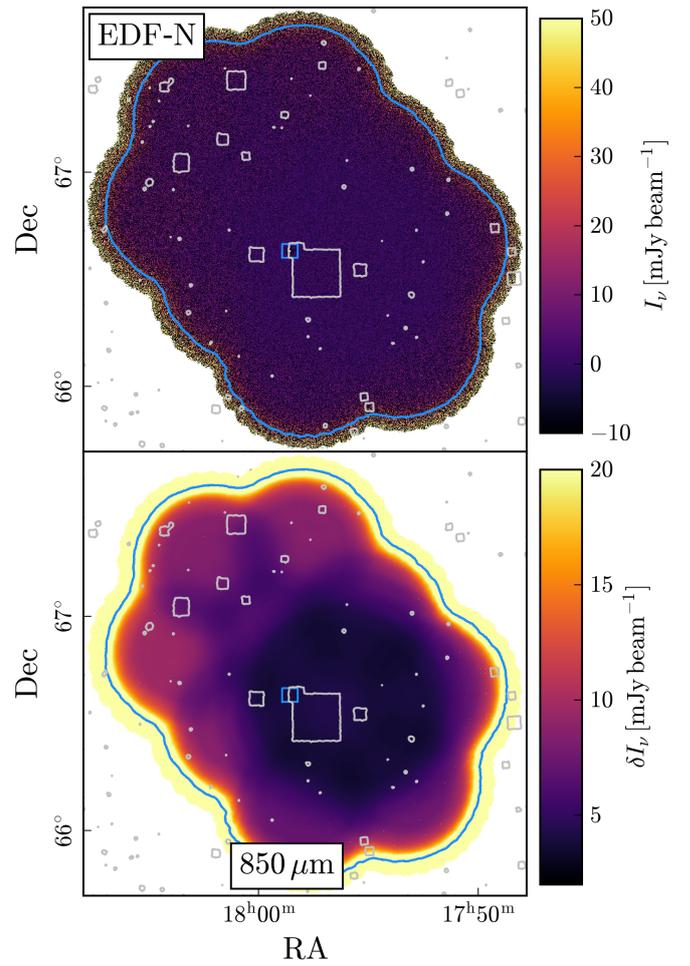
Fig. A.2: Same as Fig. 1 but for the SCUBA-2 observations of the AKARI-NEP (EDF-N) field.

mJy) in the left column and the S/N in the right column. The corresponding stacked flux densities (the value of the central pixel in the 2D cross-correlations) are provided in Table B.1. Bins that are $> 95\%$ complete in stellar mass (Euclid Collaboration: Enia et al. 2025) are highlighted in blue. The 2D cross-correlation profiles are expected to follow the autocorrelations of the instrumental beams. We tested this by computing the averaged 1D radial profiles and compared these to the expected PSF profiles. We found good agreement between the stacked signals and the PSFs for most bins with $\log_{10}(M_*/M_\odot) > 9.9$. Below this stellar mass we found that the 2D profiles can be more extended than the beam, with the largest effect seen at $500\,\mu$m where the PSF is largest. However, this does not affect the calculations and results in this work so we do not attempt to correct for it.
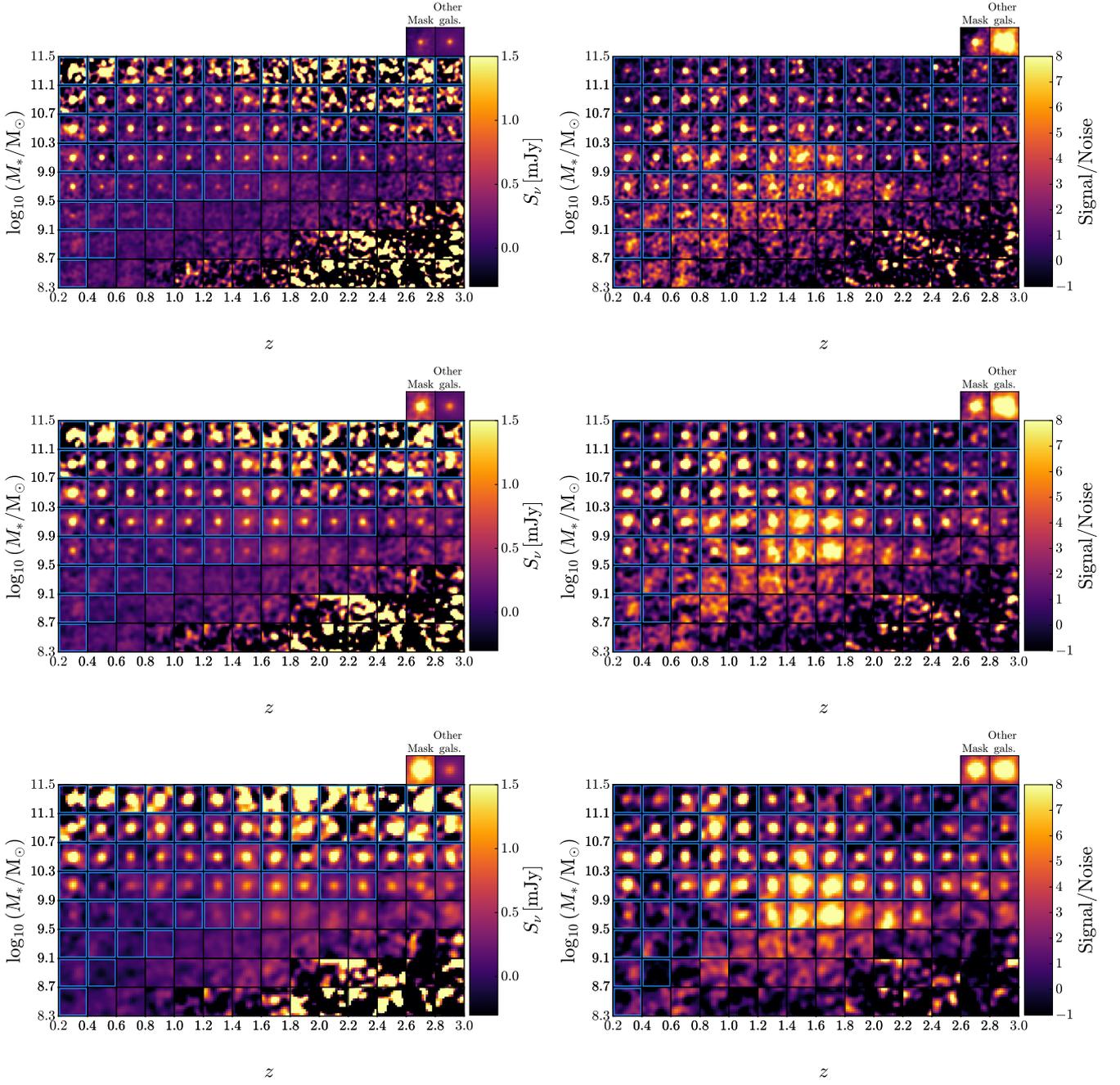
Fig. B.1: *Herschel*-SPIRE results from stacking star-forming MS galaxies from the *Euclid* catalogue (Euclid Collaboration: Enia et al. 2025) with redshifts between 0.2 and 3.0, and stellar masses between $\log_{10}(M_*/M_\odot) = 8.3$ and 11.5. Each 2D cutout is $200'' \times 200''$. Bins that are > 95% complete in stellar mass (Euclid Collaboration: Enia et al. 2025) are highlighted in blue. *Left column:* Stacking signal in units of mJy. *Right column:* The S/N of the stacked flux densities. The 'Mask' and 'Other gals.' panels differ from the colourbar and range from S/N = −1 to S/N = 60. *Top row:* SPIRE 250-μm. *Middle row:* SPIRE 350-μm. *Bottom row:* SPIRE 500-μm.
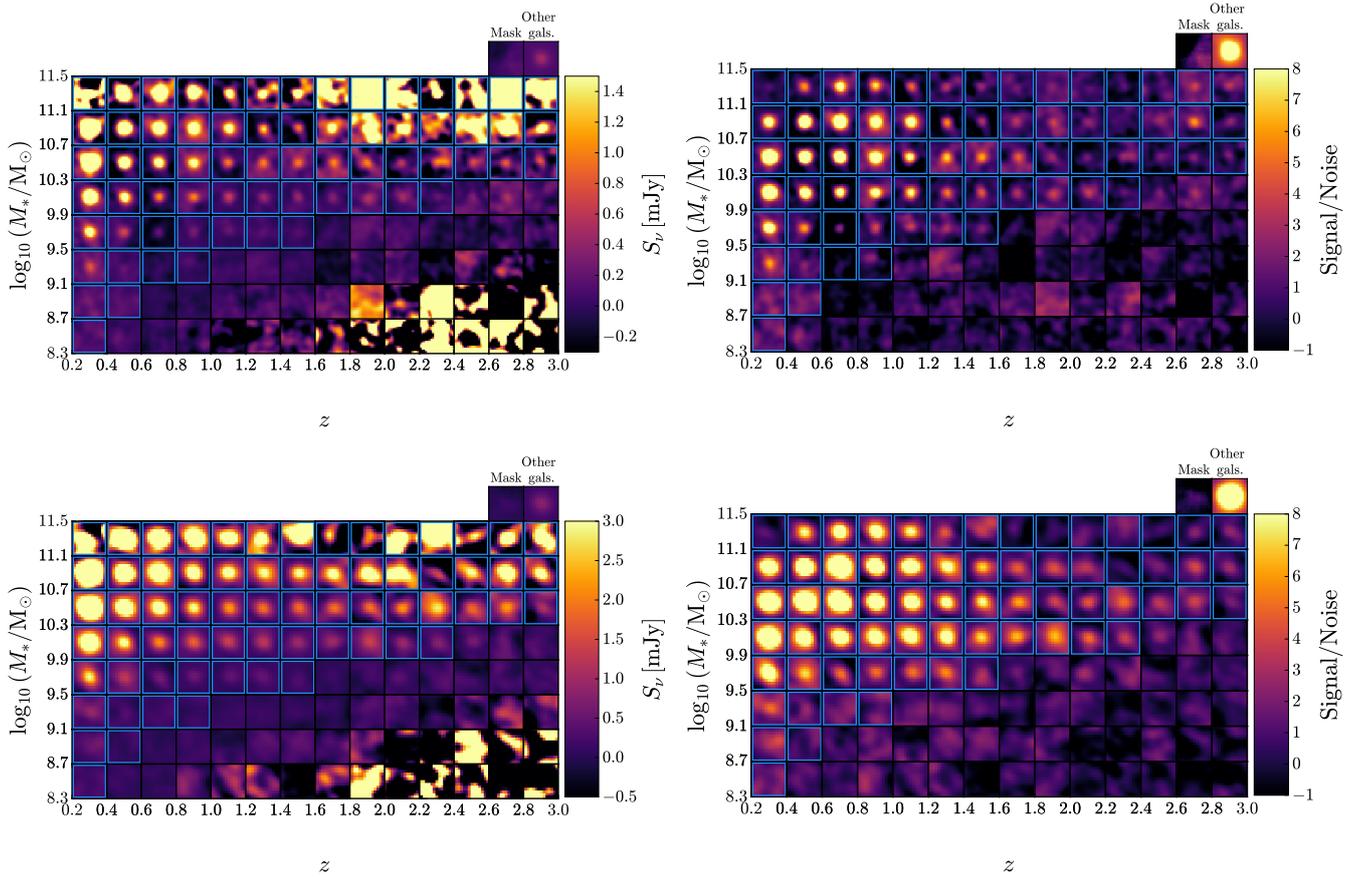
Fig. B.2: Same as Fig. B.1 but for PACS 100 (top row) and $160\,\mu$m (bottom row), and here each 2D cutout is $40'' \times 40''$. The 'Mask' and 'Other gals.' panels differ from the colourbar and range from S/N $= -1$ to S/N $= 20$.
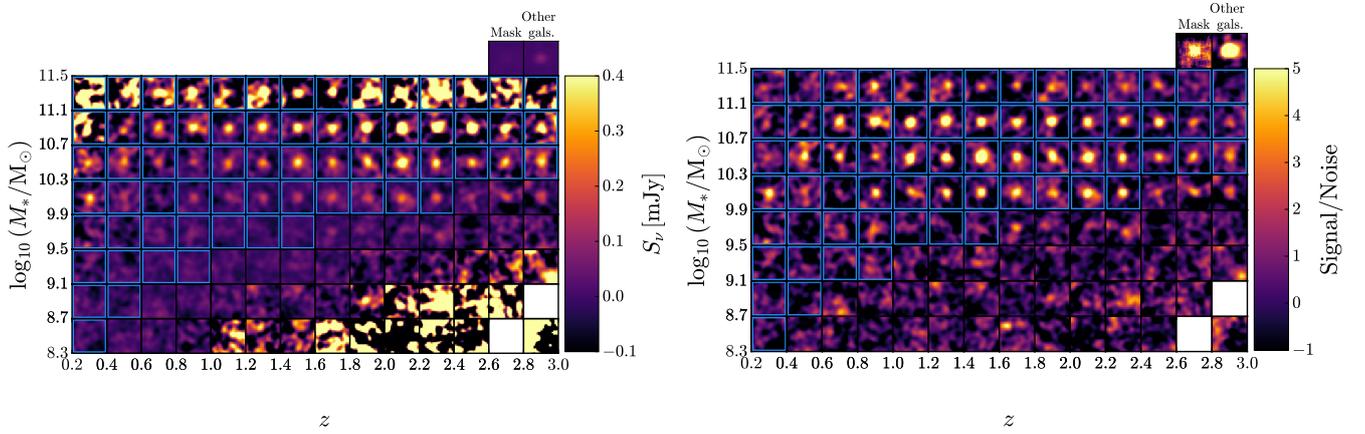
Fig. B.3: Same as Fig. B.1 but for SCUBA-2 $850\,\mu$m, and here each 2D cutout is $70'' \times 70''$.

Table B.1: Results from stacking the *Euclid* catalogue galaxies with reliable redshifts and stellar masses on the *Herschel* and SCUBA-2 images at 100, 160, 250, 350, 500, and 850 μm. The central stellar mass and redshift of each bin are given in the first two columns. The last three columns give the total number of *Euclid* galaxies in the stacking bin for the PACS, SPIRE, and SCUBA-2 images, respectively.

$\log_{10}$ $(M_*/M_\odot)$	z	S_{100} [mJy]	S_{160} [mJy]	S_{250} [mJy]	S_{350} [mJy]	S_{500} [mJy]	S_{850} [mJy]	$N_{\rm PACS}$	$N_{\rm SPIRE}$	$N_{\rm S2}$
8.5	0.3	0.06±0.09	0.16±0.13	0.16±0.07	0.16±0.06	−0.11±0.06	−0.01±0.03	17711	26737	3098
8.5	0.5	0.11±0.07	0.10±0.11	0.20±0.05	0.20±0.05	0.06±0.05	0.03±0.03	22283	33265	3622
8.5	0.7	−0.04±0.08	0.03±0.13	0.03±0.05	0.03±0.05	−0.11±0.06	−0.02±0.03	16637	26712	3537
8.5	0.9	−0.23±0.19	0.52±0.29	0.42±0.13	0.42±0.13	0.28±0.13	−0.04±0.07	3585	6146	893
8.5	1.1	−0.32±0.46	0.89±0.71	1.54±0.34	1.54±0.30	0.20±0.26	0.06±0.24	542	726	58
8.5	1.3	−0.02±0.53	0.04±0.81	0.08±0.38	0.08±0.41	−0.49±0.39	−0.02±0.21	452	656	78
8.5	1.5	0.16±0.44	−0.98±0.65	0.03±0.33	0.03±0.29	0.04±0.33	0.01±0.18	729	1038	120
8.5	1.7	−0.32±1.01	1.04±1.55	1.34±0.53	1.34±0.66	1.97±0.65	0.06±0.46	97	176	19
8.5	1.9	−1.63±3.31	4.56±5.24	1.40±0.94	1.40±1.04	0.75±1.02	0.03±1.33	7	16	1
8.5	2.1	−6.57±4.18	−1.87±5.87	−4.81±1.26	−4.81±1.20	−4.88±1.22	−1.44±0.96	4	7	2
8.5	2.3	8.31±7.30	2.23±12.65	−0.80±1.41	−0.80±1.49	−2.64±1.47	−0.55±1.37	2	9	2
8.5	2.5	−6.91±4.08	−1.53±5.96	−2.75±1.33	−2.75±1.45	−1.52±1.55	−1.37±1.18	4	14	2
8.5	2.7	3.57±6.04	−7.76±9.61	−4.93±1.97	−4.93±2.04	−3.32±2.20	...	2	4	0
8.5	2.9	−2.48±4.06	−11.68±6.31	−2.74±1.16	−2.74±1.43	−4.05±1.20	−5.97±5.65	6	6	1
8.9	0.3	0.30±0.10	0.50±0.15	0.43±0.08	0.43±0.07	0.07±0.07	0.02±0.04	13464	20832	2485
8.9	0.5	0.16±0.08	0.02±0.11	0.17±0.05	0.17±0.06	−0.21±0.06	−0.03±0.03	23380	34784	3730
8.9	0.7	−0.03±0.06	−0.02±0.09	−0.03±0.04	−0.03±0.03	−0.23±0.04	0.04±0.02	32056	54852	7937
8.9	0.9	−0.07±0.07	0.12±0.10	0.25±0.04	0.25±0.04	0.18±0.05	−0.01±0.02	26080	42735	5554
8.9	1.1	0.10±0.11	−0.04±0.16	0.15±0.08	0.15±0.08	0.00±0.08	−0.04±0.05	11300	15511	1507
8.9	1.3	0.04±0.13	0.33±0.18	0.44±0.09	0.44±0.09	0.25±0.09	−0.02±0.06	8134	11553	1147
8.9	1.5	0.08±0.14	0.42±0.20	0.46±0.09	0.46±0.10	0.46±0.12	−0.02±0.05	8304	11868	1319
8.9	1.7	0.19±0.20	0.23±0.29	0.14±0.13	0.14±0.14	0.19±0.15	−0.03±0.07	3493	6282	959
8.9	1.9	1.17±0.42	0.46±0.61	−0.13±0.24	−0.13±0.27	−0.58±0.29	0.44±0.16	730	1164	156
8.9	2.1	0.91±0.86	−0.84±1.32	0.17±0.43	0.17±0.47	−0.16±0.47	0.00±0.34	138	203	21
8.9	2.3	4.47±2.60	−3.06±3.72	−1.32±0.65	−1.32±0.69	−0.39±0.76	0.66±0.46	12	98	19
8.9	2.5	−0.49±2.81	3.00±4.27	−2.20±0.83	−2.20±0.90	−0.90±0.87	0.66±0.65	9	43	10
8.9	2.7	−2.96±2.00	−1.46±3.13	−0.20±0.91	−0.20±1.00	−1.95±0.83	−0.46±0.66	22	56	12
8.9	2.9	−1.17±3.44	−9.10±5.32	−8.45±1.13	−8.45±1.28	−1.70±1.07	...	7	10	0
9.3	0.3	0.83±0.13	0.91±0.18	0.93±0.10	0.93±0.09	−0.12±0.09	0.07±0.04	8614	13669	1740
9.3	0.5	0.21±0.09	0.33±0.13	0.41±0.06	0.41±0.07	−0.06±0.06	0.00±0.03	16626	24633	2664
9.3	0.7	0.02±0.07	0.18±0.11	0.27±0.04	0.27±0.04	−0.03±0.05	0.00±0.02	25346	43919	6410
9.3	0.9	0.03±0.06	0.08±0.08	0.35±0.04	0.35±0.04	0.10±0.04	0.02±0.02	34386	59915	8713
9.3	1.1	0.05±0.05	0.13±0.08	0.26±0.04	0.26±0.05	0.10±0.04	0.04±0.02	39345	58955	6907
9.3	1.3	0.10±0.05	0.15±0.08	0.27±0.03	0.27±0.04	0.14±0.04	0.03±0.02	44484	66271	7823
9.3	1.5	0.04±0.07	0.16±0.11	0.31±0.05	0.31±0.05	0.15±0.05	0.06±0.02	27452	50678	8247
9.3	1.7	−0.20±0.09	0.09±0.14	0.47±0.07	0.47±0.07	0.39±0.07	0.02±0.04	16232	25556	3196
9.3	1.9	−0.08±0.17	0.31±0.25	0.34±0.12	0.34±0.11	0.40±0.12	−0.06±0.06	5500	8718	1069
9.3	2.1	0.07±0.19	0.13±0.27	0.22±0.12	0.22±0.15	0.10±0.15	−0.02±0.08	4698	6887	732
9.3	2.3	−0.06±0.25	−0.12±0.39	0.41±0.17	0.41±0.21	0.11±0.20	−0.03±0.10	2001	3385	424
9.3	2.5	0.20±0.36	−0.19±0.54	0.52±0.26	0.52±0.32	0.20±0.27	−0.04±0.13	1060	1760	231
9.3	2.7	0.38±0.61	1.36±0.93	0.77±0.44	0.77±0.45	−0.22±0.48	0.06±0.17	330	651	121
9.3	2.9	−0.88±0.62	0.22±0.99	0.41±0.45	0.41±0.50	0.13±0.52	0.23±0.21	306	559	104
9.7	0.3	2.26±0.16	3.04±0.22	3.00±0.10	3.00±0.11	0.53±0.09	0.11±0.05	4893	8120	1113
9.7	0.5	0.75±0.11	1.28±0.17	1.28±0.08	1.28±0.08	−0.09±0.08	−0.05±0.04	9545	14595	1648
9.7	0.7	0.24±0.08	0.60±0.12	1.03±0.07	1.03±0.06	0.04±0.06	0.07±0.03	16956	27321	3673
9.7	0.9	0.30±0.07	0.56±0.11	0.90±0.05	0.90±0.04	0.14±0.06	0.08±0.02	22923	40925	6018
9.7	1.1	0.22±0.06	0.45±0.09	0.88±0.04	0.88±0.05	0.35±0.04	0.04±0.02	32854	51898	6737
9.7	1.3	0.18±0.06	0.49±0.09	0.77±0.03	0.77±0.04	0.48±0.04	−0.00±0.02	36846	59350	8295
9.7	1.5	0.15±0.06	0.28±0.09	0.89±0.04	0.89±0.04	0.62±0.04	0.03±0.02	33404	64649	11275
9.7	1.7	0.05±0.07	0.19±0.10	0.84±0.05	0.84±0.06	0.79±0.05	0.11±0.03	27613	43866	5555
9.7	1.9	0.20±0.10	0.22±0.15	0.55±0.08	0.55±0.08	0.58±0.08	0.02±0.04	14264	24471	3590
9.7	2.1	0.13±0.09	0.37±0.14	0.69±0.06	0.69±0.08	0.59±0.07	0.07±0.04	17092	27020	3492
9.7	2.3	−0.09±0.10	0.28±0.15	0.60±0.08	0.60±0.09	0.70±0.09	0.04±0.04	12021	18856	2400
9.7	2.5	−0.09±0.14	0.10±0.22	0.26±0.13	0.26±0.12	0.31±0.13	−0.02±0.06	7219	11203	1453
9.7	2.7	−0.04±0.19	0.11±0.28	0.96±0.17	0.96±0.16	0.54±0.15	0.04±0.06	4156	7323	1141
9.7	2.9	0.04±0.19	0.12±0.28	0.50±0.17	0.50±0.16	0.67±0.16	0.00±0.08	4087	6550	922

Continued on next page.

Table B.1 – continued from previous page.

$\log_{10}$ $(M_*/M_\odot)$	z	S_{100} [mJy]	S_{160} [mJy]	S_{250} [mJy]	S_{350} [mJy]	S_{500} [mJy]	S_{850} [mJy]	N_{PACS}	N_{SPIRE}	N_{S2}
10.1	0.3	5.43±0.21	7.67±0.32	7.18±0.16	7.18±0.12	1.48±0.11	0.41±0.07	2877	4714	593
10.1	0.5	2.23±0.15	3.29±0.22	3.84±0.09	3.84±0.09	0.61±0.08	0.16±0.05	5557	8823	1097
10.1	0.7	1.16±0.10	2.18±0.15	3.05±0.06	3.05±0.07	0.69±0.07	0.09±0.04	11363	17957	2305
10.1	0.9	1.07±0.09	1.79±0.14	2.65±0.06	2.65±0.07	0.88±0.07	0.17±0.03	13094	23321	3540
10.1	1.1	0.69±0.08	1.41±0.12	2.14±0.06	2.14±0.05	0.76±0.06	0.13±0.03	18424	30049	4223
10.1	1.3	0.46±0.08	1.27±0.12	2.14±0.06	2.14±0.06	1.05±0.06	0.16±0.03	16999	29549	4702
10.1	1.5	0.45±0.09	0.99±0.13	1.94±0.06	1.94±0.07	1.16±0.06	0.16±0.03	16666	33086	5827
10.1	1.7	0.36±0.11	1.01±0.15	2.03±0.08	2.03±0.08	1.42±0.08	0.20±0.04	12959	22961	3490
10.1	1.9	0.54±0.14	1.33±0.21	1.65±0.11	1.65±0.11	1.39±0.11	0.18±0.04	6590	13943	2519
10.1	2.1	0.51±0.13	0.97±0.19	1.66±0.11	1.66±0.12	1.14±0.10	0.26±0.04	8978	16621	2796
10.1	2.3	0.22±0.14	0.77±0.21	1.73±0.09	1.73±0.11	1.40±0.11	0.24±0.04	7396	14279	2502
10.1	2.5	0.34±0.16	0.61±0.24	1.38±0.13	1.38±0.12	1.18±0.13	0.15±0.05	6408	12037	2043
10.1	2.7	0.54±0.17	0.50±0.25	1.21±0.13	1.21±0.13	1.24±0.15	0.22±0.05	4815	10184	1896
10.1	2.9	0.08±0.16	0.23±0.24	1.01±0.12	1.01±0.14	0.97±0.15	0.17±0.06	6051	10639	1787
10.5	0.3	12.95±0.45	16.11±0.66	14.24±0.44	14.24±0.25	3.00±0.22	0.35±0.14	1126	1873	194
10.5	0.5	3.90±0.18	6.50±0.26	7.84±0.11	7.84±0.10	1.81±0.09	0.32±0.06	3398	5476	725
10.5	0.7	2.58±0.13	4.65±0.18	6.20±0.09	6.20±0.09	1.33±0.08	0.23±0.04	6785	10793	1358
10.5	0.9	2.01±0.13	3.16±0.20	4.92±0.09	4.92±0.09	1.44±0.08	0.20±0.04	6464	11564	1728
10.5	1.1	1.04±0.11	2.28±0.16	3.85±0.08	3.85±0.07	1.31±0.07	0.29±0.04	8955	15278	2356
10.5	1.3	1.04±0.14	1.96±0.20	4.10±0.09	4.10±0.10	1.70±0.10	0.31±0.04	6475	12375	2230
10.5	1.5	1.03±0.15	1.88±0.23	3.64±0.12	3.64±0.10	2.16±0.11	0.43±0.04	5409	12493	2515
10.5	1.7	1.04±0.21	1.90±0.30	3.99±0.14	3.99±0.17	2.64±0.16	0.36±0.05	2905	7341	1540
10.5	1.9	1.07±0.37	1.80±0.49	4.46±0.26	4.46±0.23	2.69±0.26	0.42±0.07	1030	3848	940
10.5	2.1	0.64±0.32	2.27±0.49	3.88±0.27	3.88±0.25	2.74±0.24	0.59±0.08	1276	3520	827
10.5	2.3	1.06±0.38	2.85±0.56	3.72±0.28	3.72±0.29	2.43±0.23	0.45±0.08	892	3264	822
10.5	2.5	0.72±0.37	1.83±0.51	3.74±0.26	3.74±0.28	2.43±0.26	0.39±0.08	1025	2968	717
10.5	2.7	0.90±0.39	2.26±0.56	2.74±0.28	2.74±0.31	2.09±0.31	0.39±0.08	834	2857	715
10.5	2.9	0.78±0.38	1.11±0.56	2.41±0.27	2.41±0.31	2.27±0.30	0.40±0.10	918	2498	558
10.9	0.3	20.03±1.63	25.09±1.58	20.58±1.28	20.58±0.70	3.55±0.49	0.52±0.31	171	289	31
10.9	0.5	5.99±0.29	9.46±0.44	12.01±0.22	12.01±0.21	2.45±0.17	0.22±0.10	1215	2106	270
10.9	0.7	4.10±0.19	7.65±0.28	9.82±0.12	9.82±0.12	2.74±0.11	0.37±0.06	2703	4678	666
10.9	0.9	2.90±0.21	5.14±0.30	8.02±0.13	8.02±0.10	2.83±0.10	0.52±0.06	2578	4614	693
10.9	1.1	2.18±0.17	3.93±0.26	6.52±0.13	6.52±0.10	2.61±0.10	0.44±0.05	3453	6049	982
10.9	1.3	1.41±0.24	3.14±0.34	4.81±0.17	4.81±0.16	2.46±0.16	0.48±0.06	2029	4407	872
10.9	1.5	1.03±0.30	3.21±0.45	5.34±0.21	5.34±0.21	2.94±0.19	0.62±0.07	1353	3595	766
10.9	1.7	2.07±0.59	3.52±0.74	5.69±0.36	5.69±0.40	3.48±0.25	0.52±0.08	443	2027	588
10.9	1.9	3.12±0.81	4.62±1.06	6.57±0.44	6.57±0.50	4.33±0.48	0.92±0.11	191	1144	369
10.9	2.1	2.83±1.06	4.76±1.37	7.68±0.72	7.68±0.73	3.97±0.79	0.98±0.15	118	709	223
10.9	2.3	0.88±1.26	1.42±1.57	3.81±0.73	3.81±0.72	2.31±0.65	0.94±0.18	83	647	189
10.9	2.5	3.26±1.19	3.16±1.54	6.64±0.79	6.64±0.82	4.68±0.78	0.93±0.16	122	638	188
10.9	2.7	6.06±0.94	5.56±1.34	6.26±0.77	6.26±0.74	2.77±0.67	0.71±0.18	153	668	171
10.9	2.9	2.52±0.99	4.05±1.37	6.77±0.68	6.77±0.84	4.66±0.66	0.58±0.20	149	510	124
11.3	0.3	6.57±5.51	6.64±6.06	18.83±2.87	18.83±1.62	6.45±1.17	1.00±0.64	14	33	7
11.3	0.5	7.76±1.21	15.02±1.80	15.42±1.04	15.42±1.08	4.42±0.81	0.64±0.41	125	217	27
11.3	0.7	5.92±0.54	9.96±0.80	15.07±0.48	15.07±0.38	4.34±0.31	0.63±0.17	399	704	113
11.3	0.9	4.01±0.52	8.21±0.72	12.59±0.33	12.59±0.28	5.07±0.27	0.87±0.16	413	776	121
11.3	1.1	2.26±0.44	5.70±0.67	10.75±0.35	10.75±0.31	4.23±0.21	0.40±0.16	523	938	119
11.3	1.3	2.27±0.65	4.58±1.01	8.77±0.53	8.77±0.51	4.67±0.51	0.84±0.21	248	542	102
11.3	1.5	2.72±0.94	4.98±1.32	9.73±0.61	9.73±0.59	5.09±0.46	0.73±0.18	141	435	112
11.3	1.7	3.17±1.76	1.81±2.17	6.57±1.10	6.57±0.85	3.43±0.80	0.78±0.19	46	294	99
11.3	1.9	5.47±2.39	2.08±2.82	9.92±1.25	9.92±1.12	6.25±1.10	1.08±0.26	26	176	52
11.3	2.1	3.26±3.34	5.98±4.06	5.98±2.14	5.98±1.62	5.67±1.74	1.17±0.46	12	106	24
11.3	2.3	4.16±2.90	6.33±3.28	12.13±1.79	12.13±1.52	6.34±1.35	1.34±0.42	21	129	36
11.3	2.5	2.10±2.33	2.67±3.13	6.84±1.23	6.84±1.33	3.54±1.29	1.72±0.44	26	121	29
11.3	2.7	9.51±2.36	6.82±2.85	11.01±1.64	11.01±1.52	5.06±1.49	0.80±0.44	34	138	30
11.3	2.9	7.20±2.01	7.09±2.72	9.80±1.24	9.80±1.64	3.44±1.41	0.32±0.48	34	104	20

Appendix C: Best-fit far-IR SED parameters and derived quantities

Here we show the resulting physical parameters T_d, M_d, and SFR in each of the stellar mass and redshift bins where we have sufficient stacked photometry to derive these physical parameters, and we provide the best-fit SED parameters and derived physical quantities. Fig. C.1 shows the physical parameters for each redshift and stellar mass bin in our stacking analysis (where bins that are $> 95\%$ complete in stellar mass are highlighted in blue – see Euclid Collaboration: Enia et al. 2025.), and best-fit far-IR SED parameters and derived parameters are provided in Table C.1. We omit showing the lowest stellar mass bins since they contain no data.
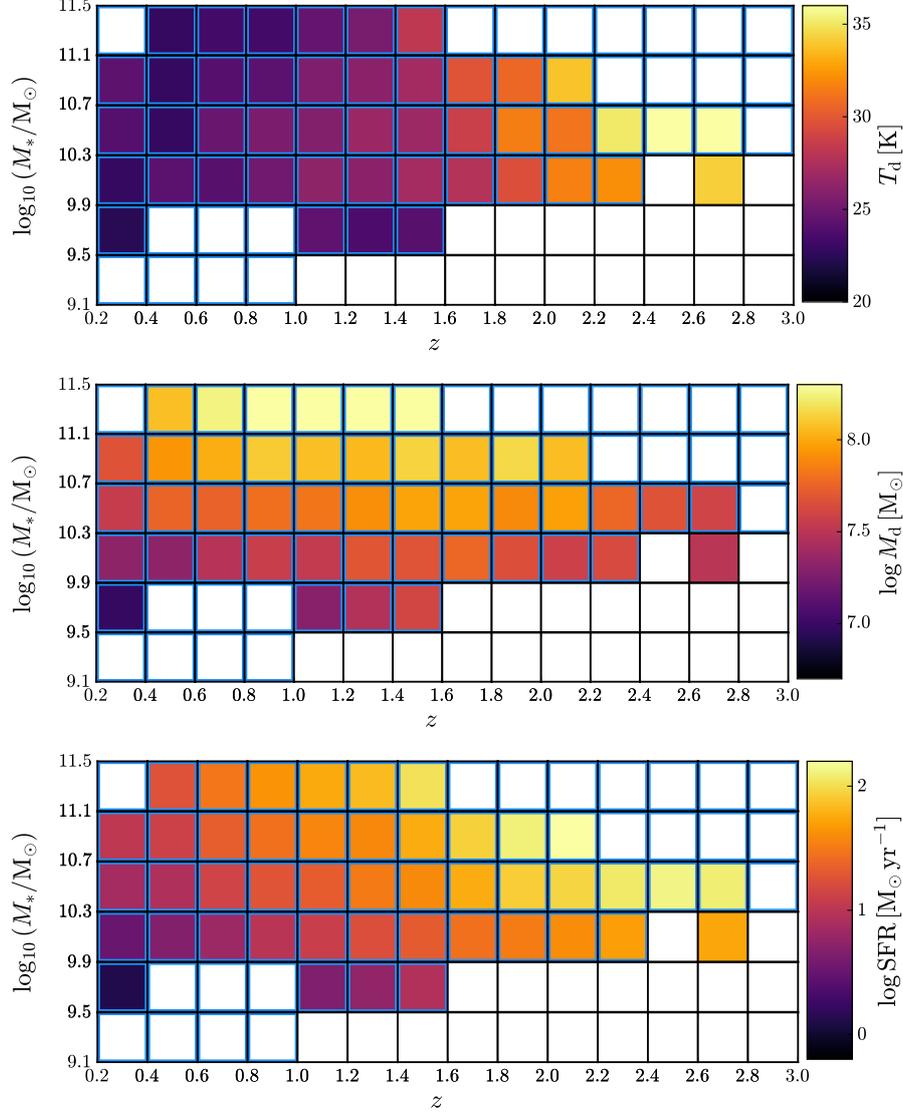
Fig. C.1: Physical parameters derived from the best-fit modified blackbody SEDs in Fig. 3. Bins that are $> 95\%$ complete in stellar mass (Euclid Collaboration: Enia et al. 2025) are highlighted in blue. *Top:* Best-fit dust temperatures, T_d. *Middle:* Dust mass (M_d), calculated by scaling the best-fit amplitude (see e.g., Reuter et al. 2020; Eales & Ward 2024; Jolly et al. 2025). *Bottom:* SFRs, calculated from L_{IR} (the integral of the best-fit SED from 8 to 1000 μm) multiplied by a factor of $1.49 \times 10^{-10} \, M_\odot \, \text{yr}^{-1} \, L_\odot^{-1}$.

Table C.1: Best-fit far-IR SED parameters (see Sect. 4.2). The central stellar mass and redshift of each bin are given in the first two columns. The amplitude A and dust temperature $T_{\rm d}$ come directly from the SED fit, while the dust mass $M_{\rm d}$ and SFR are calculated from the fit parameters.

$\log_{10}$ $(M_*/M_\odot)$	z	A $[10^{-17}]$	$T_{\rm d}$ [K]	$M_{\rm d}$ $[10^7\,M_\odot]$	SFR $[M_\odot\,{\rm yr}^{-1}]$
8.5	0.3	...	...	...	...
8.5	0.5	...	...	...	...
8.5	0.7	...	...	...	...
8.5	0.9	...	...	...	...
8.5	1.1	...	...	...	...
8.5	1.3	...	...	...	...
8.5	1.5	...	...	...	...
8.5	1.7	...	...	...	...
8.5	1.9	...	...	...	...
8.5	2.1	...	...	...	...
8.5	2.3	...	...	...	...
8.5	2.5	...	...	...	...
8.5	2.7	...	...	...	...
8.5	2.9	...	...	...	...
8.9	0.3	...	...	...	...
8.9	0.5	...	...	...	...
8.9	0.7	...	...	...	...
8.9	0.9	...	...	...	...
8.9	1.1	...	...	...	...
8.9	1.3	...	...	...	...
8.9	1.5	...	...	...	...
8.9	1.7	...	...	...	...
8.9	1.9	...	...	...	...
8.9	2.1	...	...	...	...
8.9	2.3	...	...	...	...
8.9	2.5	...	...	...	...
8.9	2.7	...	...	...	...
8.9	2.9	...	...	...	...
9.3	0.3	...	...	...	...
9.3	0.5	...	...	...	...
9.3	0.7	...	...	...	...
9.3	0.9	...	...	...	...
9.3	1.1	...	...	...	...
9.3	1.3	...	...	...	...
9.3	1.5	...	...	...	...
9.3	1.7	...	...	...	...
9.3	1.9	...	...	...	...
9.3	2.1	...	...	...	...
9.3	2.3	...	...	...	...
9.3	2.5	...	...	...	...
9.3	2.7	...	...	...	...
9.3	2.9	...	...	...	...
9.7	0.3	59.35±4.82	22.3±0.4	1.0±0.3	1.3±0.2
9.7	0.5	...	...	...	...
9.7	0.7	...	...	...	...
9.7	0.9	...	...	...	...
9.7	1.1	5.43±0.89	24.3±0.9	2.0±0.6	4.5±1.3
9.7	1.3	5.34±0.84	23.6±0.7	2.9±0.9	5.7±1.3
9.7	1.5	5.14±0.74	24.1±0.7	4.0±1.2	8.6±2.0
9.7	1.7	...	...	...	...
9.7	1.9	...	...	...	...
9.7	2.1	...	...	...	...
9.7	2.3	...	...	...	...
9.7	2.5	...	...	...	...
9.7	2.7	...	...	...	...
9.7	2.9	...	...	...	...
10.1	0.3	131.04±5.78	22.8±0.2	2.1±0.6	3.2±0.3

Table C.1 – continued from previous page.

log$_{10}$ ($M_*/M_\odot$)	z	A [10^{-17}]	T_d [K]	M_d [10^7 M$_\odot$]	SFR [M$_\odot$ yr^{-1}]
10.1	0.5	39.39±2.58	24.2±0.4	2.1±0.6	4.7±0.5
10.1	0.7	25.35±1.74	24.1±0.4	3.1±0.8	6.5±0.8
10.1	0.9	16.30±1.21	25.0±0.4	3.6±1.0	9.8±1.3
10.1	1.1	9.42±0.70	26.2±0.4	3.4±0.9	12±2
10.1	1.3	8.78±0.70	26.1±0.5	4.8±1.3	17±2
10.1	1.5	6.09±0.54	27.1±0.5	4.8±1.3	20±3
10.1	1.7	5.38±0.55	27.7±0.6	5.7±1.6	28±5
10.1	1.9	3.22±0.48	29.5±0.9	4.5±1.3	32±8
10.1	2.1	2.08±0.32	31.5±1.0	3.7±1.1	39±10
10.1	2.3	1.92±0.25	32.0±0.9	4.3±1.2	49±11
10.1	2.5	. . .	. . .	. . .	. . .
10.1	2.7	0.96±0.20	34.2±1.5	3.1±1.0	54±18
10.1	2.9	. . .	. . .	. . .	. . .
10.5	0.3	217.31±10.24	24.0±0.2	3.5±0.9	7.3±0.6
10.5	0.5	104.44±4.20	22.8±0.2	5.6±1.5	8.6±0.6
10.5	0.7	45.94±1.93	24.7±0.2	5.5±1.5	14±1
10.5	0.9	27.55±1.47	25.5±0.3	6.1±1.6	18±2
10.5	1.1	17.88±1.04	25.8±0.3	6.5±1.7	21±2
10.5	1.3	14.51±1.03	26.7±0.4	8.0±2.2	32±4
10.5	1.5	12.21±0.93	26.8±0.5	9.6±2.6	38±5
10.5	1.7	8.93±0.88	28.7±0.6	9.5±2.6	57±9
10.5	1.9	5.59±0.77	31.5±1.0	7.8±2.3	82±18
10.5	2.1	5.17±0.74	31.1±1.0	9.2±2.7	90±19
10.5	2.3	2.59±0.42	35.0±1.3	5.8±1.8	113±33
10.5	2.5	1.72±0.30	37.2±1.4	4.7±1.5	132±36
10.5	2.7	1.19±0.27	37.9±1.8	3.9±1.3	122±47
10.5	2.9	. . .	. . .	. . .	. . .
10.9	0.3	293.26±28.24	24.3±0.5	4.7±1.3	11±2
10.9	0.5	158.19±7.67	22.8±0.3	8.5±2.2	13±1
10.9	0.7	84.67±3.13	24.0±0.2	10.2±2.7	22±1
10.9	0.9	57.28±2.52	24.2±0.3	12.8±3.4	28±2
10.9	1.1	31.88±1.59	25.6±0.3	11.6±3.1	36±3
10.9	1.3	20.18±1.86	26.1±0.5	11.1±3.1	38±6
10.9	1.5	17.10±1.70	27.0±0.6	13.4±3.7	57±9
10.9	1.7	10.81±1.41	29.8±0.9	11.5±3.3	86±20
10.9	1.9	10.03±1.50	30.6±1.0	14.0±4.2	124±31
10.9	2.1	6.43±1.34	33.8±1.6	11.5±3.8	183±67
10.9	2.3	. . .	. . .	. . .	. . .
10.9	2.5	. . .	. . .	. . .	. . .
10.9	2.7	. . .	. . .	. . .	. . .
10.9	2.9	. . .	. . .	. . .	. . .
11.3	0.3	. . .	. . .	. . .	. . .
11.3	0.5	216.49±35.47	22.7±0.8	11.6±3.6	18±5
11.3	0.7	145.44±10.79	23.3±0.4	17.5±4.7	31±4
11.3	0.9	109.95±7.87	23.3±0.4	24.5±6.6	43±5
11.3	1.1	61.73±5.11	24.6±0.5	22.5±6.1	55±8
11.3	1.3	41.94±6.66	25.3±0.9	23.1±7.0	67±18
11.3	1.5	24.91±3.86	28.1±1.0	19.5±5.9	105±27
11.3	1.7	. . .	. . .	. . .	. . .
11.3	1.9	. . .	. . .	. . .	. . .
11.3	2.1	. . .	. . .	. . .	. . .
11.3	2.3	. . .	. . .	. . .	. . .
11.3	2.5	. . .	. . .	. . .	. . .
11.3	2.7	. . .	. . .	. . .	. . .
11.3	2.9	. . .	. . .	. . .	. . .